JM PAPERS

Temporal decay of secondary motions in turbulent channel flows

A. Andreolli[1,2] , **N. Hutchins**[2] , **B. Frohnapfel**[1] **and D. Gatti**[1]

[1]Institute of Fluid Mechanics, Karlsruhe Institute of Technology, Kaiserstraße 10, 76131 Karlsruhe, Germany

[2]Department of Mechanical Engineering, University of Melbourne, VIC 3010, Australia

Corresponding author: D. Gatti, davide.gatti@kit.edu

We perform direct numerical simulations of turbulent channel flows. Secondary motions are produced by applying a streamwise-homogeneous, spanwise-heterogeneous roughness pattern of spanwise period Λ_s to the walls of the channel; their time evolution is observed. Notice that, owing to the geometry, the secondary motions are streamwise-invariant at any instant of time, so that no spatial development is seen. Once the secondary motions reach a statistically steady state, the roughness pattern is suddenly removed, so that the secondary motions decay. The time needed for the secondary motions to vanish is then measured; in doing so, we distinguish between the streamwise-momentum pathways and the cross-sectional circulatory motions that compose the secondary motions. Larger values of Λ_s are generally associated with a longer time scale for the decay of the momentum pathways, although this might not hold true for $\Lambda_s/h > 4$ (where h is the channel half-height). The value of such a time scale for the circulatory motions, instead, saturates for $\Lambda_s/h \geqslant 2$; this may be related to the observed spatial confinement of said circulatory motions. For specific values of Λ_s ($2 \leqslant \Lambda_s/h \leqslant 4$), the volume-averaged energy associated with the momentum pathways undergoes an unexpected transient growth with respect to its value at the beginning of the decay. This might indicate that structures of such a specific size are able to self-sustain as postulated by Townsend (*The Structure of Turbulent Shear Flow*, 2nd edition, 1976, ch. 7.19); the evidence we gather in this respect is however inconclusive. Finally, the present data suggest that most of the energy of the momentum pathways is produced by the circulatory motions transporting the mean (spanwise-averaged) velocity.

Key words: turbulent boundary layers

1. Introduction

Starting from the seminal work of Nikuradse (1931), turbulent flows over rough surfaces have been commonly studied in the presence of statistically homogeneous roughness. The drag penalty induced by the imperfections of the surface is reflected in a vertical shift of the universal logarithmic velocity profile, which can be readily calculated from the equivalent sand-grain roughness (see, for instance, the review by Chung *et al.* 2021). The equivalent roughness is in turn a hydraulic quantity whose *a priori* calculation from the roughness topology is the subject of ongoing research (e.g. Flack & Schultz 2010; Yang *et al.* 2023).

However, naturally occurring rough surfaces (such as that generated by the deposition of dirt, ice or organic matter over the surface of a vehicle) can rarely be regarded as homogeneous, so that the effect they have on the flow is more complex than a vertical shift of the velocity profile. For example, Mejia-Alvarez *et al.* (2013) have inspected the roughness generated on a turbine blade by deposition of foreign materials, finding that it contained randomly distributed elements of different scales. The flow over such a multi-scale roughness has been experimentally investigated in a boundary layer wind tunnel (Mejia-Alvarez & Christensen 2013; Barros & Christensen 2014). It has been found that the ensemble-averaged velocity field is highly heterogeneous as it contains coherent regions of low and high momentum (low and high momentum pathways); these occur in the absence of obvious geometric features (e.g. ridges). As a note of caution, it is worth highlighting that the rough surface used in the mentioned studies was manufactured by aligning several identical rough plates; this creates a large-scale regularity in the surface that might favour the formation and sustainment of the observed momentum pathways. The pathways have an h-scaled extent in the streamwise and wall-normal direction, where h is the outer length scale (the boundary layer thickness for the studies mentioned here). Nikora *et al.* (2019) observed similar coherent motions over multi-scale roughness in open channel flows, finding that the pathways provide a contribution to skin friction that adds up to the direct effect of roughness. Comparable low- and high-momentum pathways were found both experimentally (Womack *et al.* 2022) and numerically (Kaminaris *et al.* 2023) by studying the turbulent flow over a random distribution of truncated conical roughness elements resembling the barnacles that accumulate on ship hulls. These pathways extend for at least $18h$ (Womack *et al.* 2022) in the streamwise direction; the position at which they occur is reproducible across different repetitions of the same experiment. Also, high- and low-momentum pathways of an h-scaled spanwise period were observed by Reynolds *et al.* (2007) in a boundary layer evolving over an array of staggered cubic roughness elements. In this last case, however, the spanwise period of the momentum pattern increased with streamwise fetch in an almost quantised manner.

There is no consensus over what triggers the formation of these momentum pathways. Kaminaris *et al.* (2023) found that the spanwise topology of the pathways correlates well with that of the leading edge of the roughness (that is, the first row of roughness elements stretching over the spanwise direction). They went on to show that the pathways are effectively triggered by the leading edge, and persist for a finite distance downstream of it regardless of whether they evolve over a smooth or a rough surface. Conversely, Barros & Christensen (2014) found a local correlation between the roughness topology and the pathways, suggesting that the pathways originate from heterogeneity in the roughness properties in a similar way to secondary motions over spanwise heterogeneous roughness. It is unclear which of these two mechanisms is dominant; it cannot be excluded that both contribute to the formation of the pathways. Nevertheless, there is a close resemblance between the pathways and secondary motions observed over spanwise heterogeneous roughness (as we will discuss below), to the point that the pathways themselves are also referred to as secondary motions. Both the pathways and the secondary motions, in turn,

have often been linked to the naturally occurring very-large-scale motions (VLSMs; see, for instance, Kim & Adrian 1999; Hutchins & Marusic 2007*a*; Lee & Moser 2018) seen in turbulent wall-bounded flows.

Spanwise heterogeneous roughness is usually studied in terms of spanwise-alternating streamwise-elongated strips with different roughness properties (Hinze 1967; Nugroho *et al.* 2013; Turk *et al.* 2014; Willingham *et al.* 2014; Anderson *et al.* 2015; Stroh *et al.* 2016; Vanderwel *et al.* 2019; Stroh *et al.* 2020; Frohnapfel *et al.* 2024). The strip width is typically indicated by s; notice that this is half the period Λ_s of the spanwise roughness pattern. The roughness pattern induces secondary motions; as long as the strips are narrow ($s \leqslant h$), the secondary motions consist in high- and low- momentum pathways flanked by cross-sectional circulatory motions (for instance, Chung *et al.* 2018). The same topology has been observed for the pathways occurring over multi-scale roughness (Barros & Christensen 2014; Nikora *et al.* 2019). Conditional views of VLSMs (Hutchins & Marusic 2007*b*; Hwang *et al.* 2016) also share the same geometry, the main difference being that VLSMs occur at random spanwise positions whereas the position of secondary motions is based on the roughness topology. It has been proposed that momentum pathways and secondary motions originate as the geometric or roughness features at the wall provide a preferential spawning position for VLSMs (Mejia-Alvarez & Christensen 2013; Chung *et al.* 2018; Wangsawijaya & Hutchins 2022). This view is corroborated by the observation that randomly occurring VLSMs do not coexist with fixed-position secondary motions of comparable size ($s/h \approx 1$, Barros & Christensen 2019; Zampiron *et al.* 2020; Schäfer 2023). Moreover, both VLSMs and secondary motions have been found to meander about their spawning position, although the associated streamwise periods are slightly different (Hutchins & Marusic 2007*a*; Kevin *et al.* 2017, 2019; Vanderwel *et al.* 2019; Wangsawijaya & Hutchins 2022). Another difference is given by the fact that VLSMs are typically observed in the log-layer, whereas secondary motions of comparable size extend to the wake region (Wangsawijaya *et al.* 2020).

One additional common property of naturally occurring VLSMs and the pathways or secondary motions is that they are often observed to have a characteristic spanwise length scale of the order of $1h$. The typical spanwise scale of VLSMs occurring over smooth walls is indeed $1 - 4\,h$ (Lee & Moser 2018), although their size is flow dependent. The momentum pathways found over multi-scale and randomly distributed roughness are also h-spaced in the spanwise direction (as can be seen from the data of Reynolds *et al.* 2007; Barros & Christensen 2014; Womack *et al.* 2022). Secondary motions induced by a spanwise roughness pattern are most energetic when the strip spacing s is of the order of h (Vanderwel & Ganapathisubramani 2015; Medjnoun *et al.* 2018; Wangsawijaya *et al.* 2020); as the strip spacing is increased to larger values ($s \gg h$), the secondary motions stop growing in size and rather remain confined to an h-wide region around roughness transitions.

There are at least two possible explanations for the frequent observation of dominant h-scaled features in turbulent flows; they are not necessarily mutually exclusive. The study of the linearised Navier–Stokes equations in wall-bounded flows has revealed that the perturbations they amplify the most are either inner- or h-scaled in the spanwise direction (Del Álamo & Jiménez 2006; Cossu *et al.* 2009; Alizard *et al.* 2015). Large-scaled perturbations evolve into structures reminiscent of the conditional views of VLSMs, of secondary motions and of the momentum pathways flanked by rolling motions, although linear analysis tends to overestimate the spanwise wavelength of these features (Alizard *et al.* 2015). Similar results have been found by searching the volume forcing mode that is most amplified by the linearised Navier–Stokes equations (Hwang & Cossu 2010; Illingworth 2020). In light of these linear amplification mechanisms, then, the

phenomenology described above can be explained as follows. A broadband disturbance (as a velocity perturbation or a volume force) is provided either by nonlinear interactions between small scales or by the roughness topology; the flow then acts to selectively amplify disturbances of a particular h-scaled set of wavelengths to yield the observed VLSMs or momentum pathways. The plausibility of this hypothesis is corroborated by evidence that channel flows are particularly sensitive to spanwise disturbances at the wall (Jovanović & Bamieh 2005). An alternative, yet similar, explanation is provided by Townsend (1976, chap. 7.19) in an attempt to explain the persistence of some h-scaled perturbations often seen in wind tunnels. Using suited approximations, Townsend estimated that spanwise variations of the wall-shear stress whose characteristic wavelength falls in a limited ($\leqslant 4h$) h-scaled range should be able to self-sustain and thus dominate the remaining flow features. It is then conceivable (as pointed out by Wangsawijaya *et al.* 2020) that a broadband perturbation could trigger a set of motions of different scales, of which some h-scaled ones would outlive the others to yield VLSMs or the h-scaled momentum pathways.

The aim of this article is to measure the persistence in time of secondary motions of different sizes once the external factors that trigger their appearance and allow for their sustainment are removed. In particular, we consider secondary motions induced by spanwise roughness patterns of different periods. This is done both in an attempt to assess the plausibility of Townsend's estimates and to investigate the streamwise-extended secondary motions observed over a smooth wall in the wake of roughness features (Kaminaris *et al.* 2023). In § 2, we explain our numerical procedure: secondary motions extracted from a steady-state flow over heterogeneous roughness are allowed to evolve in time in a channel flow with smooth walls until they decay. The theoretical framework underlying the analyses presented in this paper is then presented in § 3. An overview of the fully developed steady-state secondary motions is given in § 4; their time evolution is then tracked (§ 5) through an ensemble-average of multiple realisations of the same simulation. For completeness, we also briefly show the time evolution of near-wall streamwise fluctuations in § 6. A concluding discussion is given in § 7.

2. Problem statement and numerical method

We perform direct numerical simulation (DNS) of incompressible channel flows at constant pressure gradient (CPG). The peculiarity of this dataset is that the simulations capture the decay of secondary motions of different sizes; this process is clearly not at a statistically steady state. Rather, our simulations describe the transition from a statistically steady state (flow with secondary motions) to a second steady state (flow in a smooth channel). To still be able to compute averages, each simulation is then run several times, each time starting from a different realisation of a given statistically steady state. Ensemble averages are then calculated.

The channel geometry is shown in figure 1. Let x, y, z be the streamwise, wall-normal and spanwise directions; u, v, w are the corresponding components of the velocity vector $\boldsymbol{u}$. The flow is periodic in the streamwise and spanwise directions (periodic boundary conditions); the corresponding periods are indicated as L_x and L_z, respectively. The flow is statistically homogeneous in the streamwise direction, but not in the spanwise one: indeed, as will be discussed below, a spanwise-heterogeneous (but streamwise-homogeneous) roughness pattern at the wall induces spanwise-heterogeneities of the average flow velocity.

Time is indicated by t. At $t = 0$, the flow is at a statistically steady state in the presence of secondary motions. These are sustained by a spanwise roughness pattern consisting in
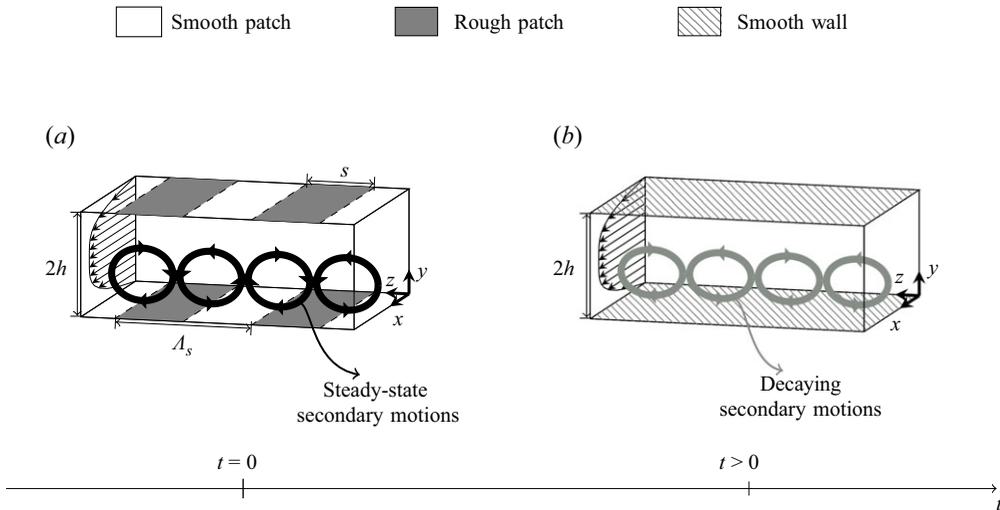
Figure 1. Schematic problem description with a graphical representation of secondary motions. The initial condition ($t = 0$) of our numerical set-up is shown in panel (*a*): steady-state secondary motions are observed over strip-type roughness. A generic point t in time (with $t > 0$) is depicted in panel (*b*): the secondary motions decay as they evolve over a smooth wall. Box size not to scale. Adapted from Neuhauser *et al.* (2022).

alternating streamwise-elongated strips of smooth and rough wall. We will refer to this set-up as strip-type roughness. The spanwise width of each strip is s; the spanwise period of the pattern is $\Lambda_s = 2s$. For $t > 0$, the spanwise roughness pattern is suddenly replaced by a smooth wall, so that the decay of the secondary motions is observed. The pressure gradient is kept constant in the process.

Notice, once again, that the flow is streamwise-homogeneous. As the strip-type roughness is removed from the walls, the flow departs from its steady state, but retains its streamwise homogeneity. In other words, the flow develops temporally, but not in the streamwise direction. Our present approach is thus similar to that of Toh & Itano (2005), in the sense that we investigate the time evolution of streamwise-invariant flow structures. Notice, moreover, that an increase of the bulk velocity is observed as a result of the removal of the strip-type roughness: as the pressure gradient is kept constant, the reduction in skin friction at the wall leads to an increase of the flow rate. Mass is conserved throughout the process: owing to the present geometry, conservation of mass only requires the average flow velocity to be streamwise-invariant, so that time variations of the flow rate are admissible.

Owing to the instationarity and spanwise heterogeneity of the problem, care must be exerted when defining averaging operators and viscous units. The operator $\langle \cdot \rangle$ indicates the expected value and is computed as an average over multiple repetitions of the same simulation, over the streamwise direction and over multiple spanwise periods of the selected geometry (phase average, see Reynolds & Hussain 1972); known symmetries in the wall-normal and spanwise directions are used to improve convergence wherever possible. The resulting statistics depend on the conditioned spanwise variable ζ and time, as well as on the wall-normal coordinate y. If an additional spanwise average is performed, the symbol $\langle \cdot \rangle_z$ is used. As for inner units, the expected value $\tau_w(t, \zeta)$ of the wall shear stress is a function of time and of the spanwise coordinate. So are the friction velocity $u_\tau(t, \zeta) = \sqrt{\tau_w/\rho}$ and the viscous length scale $\delta_v(t, \zeta) = \nu/u_\tau$, where ρ is the density and ν the kinematic viscosity. For the calculation of the worst-case inner-scaled grid spacing,

the maximum value $u_{\tau,m}$ of the friction velocity can be used:

$$u_{\tau,m} = \max_{t,\zeta} \, u_{\tau}(t, \zeta); \qquad \delta_{v,m} = \frac{\nu}{u_{\tau,m}}. \tag{2.1}$$

Leveraging the fact that the pressure gradient $-G$, $G > 0$ is forcedly kept constant during our simulations, a global friction velocity u_p and length scale δ_p can also be defined:

$$u_p = \sqrt{\frac{hG}{\rho}}; \qquad \delta_p = \frac{\nu}{u_p}. \tag{2.2}$$

Quantities scaled with these global viscous units will be indicated with a $(\cdot)^+$ superscript. They are also used for the definition of the friction Reynolds number $Re_\tau = hu_p/\nu$. The relation between global and local viscous units can be found by integrating the streamwise momentum balance of the Navier–Stokes equations. By defining the bulk velocity as the volume-average of the expected streamwise component,

$$U_b(t) = \frac{1}{2h} \int_0^{2h} \langle u \rangle_z \, \mathrm{d}y, \tag{2.3}$$

the following relation is obtained:

$$\rho h \frac{\mathrm{d}U_b}{\mathrm{d}t} = hG - \langle \tau_w \rangle_z. \tag{2.4}$$

Under steady conditions ($t = 0$ and $t \to \infty$ for the problem considered here), the global u_p is the friction velocity built by using the spanwise average $\langle \tau_w \rangle_z$ instead of τ_w in its definition:

$$u_p = \sqrt{\frac{\langle \tau_w \rangle_z}{\rho}} \qquad \text{only at a steady state.} \tag{2.5}$$

2.1. *Numerical method and details*

We perform DNS using the open-source solver Xcompact3d (Laizet & Lamballais 2009; Laizet & Li 2011; Bartholomew *et al.* 2020), using sixth-order compact finite differences in space combined with an explicit third-order Runge–Kutta scheme in time. We test different configurations for varying Λ_s at two different friction Reynolds numbers ($Re_\tau = 180$ and $Re_\tau = 500$). While the streamwise extent L_x of the simulation domain is set to values that are greater or equal to those used by Neuhauser *et al.* (2022) for analogous simulations, the spanwise box size L_z is set alternatively to $12h$, $8h$ or $6h$ to accomodate an integer, even number of strips for each of the tested values of Λ_s. The $L_z = 6h$ box size is preferred at high-Re wherever possible to minimise the computational load of a single simulation.

Our data production pipeline consists of two stages. First, initial conditions are produced by simulating a channel flow with a spanwise roughness pattern of period Λ_s (see figure 1a). Rough wall sections are modelled by imposing a slip length ℓ for the spanwise velocity component at the wall as done by Neuhauser *et al.* (2022). This results in the following Robin boundary condition:

$$w_w = \ell \, \hat{n}_w \cdot (\nabla w)_w, \tag{2.6}$$

where the $(\cdot)_w$ subscript indicates a quantity evaluated at the wall, $\hat{n}_w$ a unit vector that is orthogonal to the wall and pointing into the fluid. The value of the slip length is set to $\ell^+ = 9$ following Neuhauser *et al.* (2022). After the simulation reaches a steady state, a set of N_s snapshots is stored; the sample time is set to $1h/u_p$ to ensure that snapshots are

colour	Re_τ	Λ_s/h	N_0 or N_s	$T_f\, u_p/h$	$(L_x, L_z)/h$	$(\Delta x, \Delta z, \Delta y_c, \Delta y_w)/\delta_{v,m}$	CFL_{max}	Fo_{max}
	180	Smooth	170	N.A.	(8, 12)	(8.0, 3.75, 8.48, 0.85)	0.5350	0.1246
●	180	0.5	80	5	(8, 12)	(8.54, 4.00, 9.05, 0.91)	0.7009	0.1246
●	180	1	200	5	(8, 12)	(8.86, 4.15, 9.39, 0.94)	0.6781	0.1246
●	180	2	200	5	(8, 12)	(8.69, 4.07, 9.21, 0.92)	0.6115	0.1246
●	180	4	250	8	(8, 12)	(8.75, 4.10, 9.28, 0.93)	0.7020	0.1246
●	180	6	300	10	(8, 12)	(8.73, 4.09, 9.25, 0.93)	0.6998	0.1246
	500	Smooth	151	N.A.	(12, 6)	(10.00, 5.00, 9.76, 1.00)	0.7096	0.0700
●	500	0.5	108	3.1	(12, 6)	(10.81, 5.41, 10.56, 1.08)	0.6696	0.0700
●	500	1	162	3.5	(12, 6)	(10.85, 5.42, 10.59, 1.08)	0.6974	0.0700
●	500	2	162	5.1	(12, 6)	(10.89, 5.45, 10.63, 1.09)	0.6764	0.0700
●	500	4	165	8.2	(12, 8)	(10.96, 5.48, 10.70, 1.10)	0.7619	0.0700
●	500	6	180	8.2	(12, 6)	(10.87, 5.44, 10.61, 1.09)	0.7646	0.0700

Table 1. Numerical details for all tested combinations of Λ_s/h (the spanwise period of the roughness pattern) and Re_τ for our smooth (steady) and time-evolving simulations. The number of fields used to calculate statistics is indicated by $N_0 = N_s$ (where N_0 refers to steady-state simulations, N_s to time-evolving ones). T_f indicates the time duration of the decaying simulation, L_x and L_z refer to the simulation box size in the streamwise and spanwise directions; the grid spacing is uniform in these two directions and is indicated by Δx, Δz respectively. The wall-normal grid spacings at the wall and centreline are instead indicated by Δy_w and Δy_c. The maximum in time, over each grid point and over the three spatial directions (or velocity components) of the Courant–Friedrichs–Lewy (CFL $= V\Delta t/q$, where Δt is the simulation time step, q is the grid spacing at some generic point in a given direction and V is the velocity component at that point in the same direction) and Fourier ($Fo = \nu\Delta t/q^2$) numbers are also reported. The dot to the left of each row indicates the colour used in the following figures to indicate a given value of Λ_s/h.

reasonably uncorrelated. As previously explained, u_p is analogous to u_τ; then, if h is the maximum height of an attached eddy, its lifetime can be expected to be of the order of the eddy turnover time $1h/u_p$ (see, e.g., Lozano-Durán & Jiménez 2014). One can then expect that the turbulent features observed in a given snapshot differ from those of the successive snapshot saved after $1h/u_p$.

Each of the N_s saved snapshots of the secondary motions is used as the initial condition for a second simulation between smooth walls (see figure 1b). The duration of the simulation T_f is chosen to satisfactorily capture the decay of the secondary motions. Streamwise-averaged flow fields are stored every $0.01h/u_p$, even though a laxer time resolution could have been used in retrospect. Streamwise-averaged velocity fields are preferred to three-dimensional snapshots as the present procedure is particularly data intensive. Exploiting the several repetitions of the simulation, a total of N_s fields at the same time t from the initial conditions are averaged together to produce an ensemble-average of the decaying secondary motions. The whole procedure is repeated for different values of Λ_s and Re_τ.

Numerical details for the complete dataset used for this study are reported in table 1. The grid spacing is normalised with the worst-case value $\delta_{v,m}$ of the viscous length scale; such a value is usually observed at the initial conditions. Additionally to the decaying simulations, two reference simulations between smooth walls ($Re_\tau = 180$, $Re_\tau = 500$) have been produced using the same grid used for rough simulations. In this case, N_0 indicates the number of samples used for the calculation of steady-state statistics. Notice that we adjust the number of fields (N_s, N_0) used for the computation of statistics as we change Re_τ and Λ_s; as for the quantification of the degree of statistical convergence, see § 3.5. Generally, Re_τ has a favourable effect on the convergence of statistics: as near-wall turbulent structures become smaller with larger Re_τ, a larger number of these features are contained in a single flow snapshot. This yields a quicker falloff of the small-scale noise.

It is thus expected that a lower number of snapshots (N_s, N_0) is required for statistics to converge at high-Re_τ. The effect of the period Λ_s depends instead on the size L_z of the simulation box. As previously explained, data from the several spanwise periods contained in a single snapshot are averaged together (phase-averaging); the larger the number of periods L_z/Λ_s in a single snapshot, the lower we expect the required N_s (or N_0) to be.

3. Theoretical framework

3.1. *Triple decomposition; momentum pathways and circulatory motions*

Unlike homogeneous flows, which are best described using a Reynolds decomposition, flows featuring secondary motions are commonly described in terms of a triple decomposition. As would be done in a Reynolds decomposition, velocity fluctuations u' are separated from the expected value $\langle u \rangle$. Additionally, the expected value $\langle u \rangle$ is further split into its spanwise average $U = \langle u \rangle_z$ and a dispersive field $u_d = (\tilde{u}, \tilde{v}, \tilde{w})$ to yield the triple decomposition. This is done as the expected value $\langle u \rangle$ of the velocity depends on the conditioned spanwise variable ζ (see § 2); using the triple decomposition, the spanwise-uniform field U is separated from the spanwise-heterogeneous dispersive field u_d,

$$\langle u \rangle = U + u_d. \tag{3.1}$$

Since only the streamwise component has a non-zero spanwise average for the present geometry,

$$U = U(t, y) \,\hat{x}, \tag{3.2}$$

$$\tilde{u} = \langle u \rangle - U(t, y), \quad \tilde{v} = \langle v \rangle, \quad \tilde{w} = \langle w \rangle, \tag{3.3}$$

where $\hat{x}$ is a unit vector pointing in the streamwise direction and U will be referred to as the mean velocity profile. The full velocity field then reads

$$u(t, x, y, z) = U(t, y) \,\hat{x} + u_d(t, y, \zeta(z)) + u'(t, x, y, z). \tag{3.4}$$

Note that the averaged fields U, u_d are streamwise-invariant owing to the channel geometry. This allows to further split the dispersive field u_d into two separate parts. Indeed, the continuity equation for u_d reads

$$\frac{\partial \tilde{v}}{\partial y} + \frac{\partial \tilde{w}}{\partial \zeta} = 0. \tag{3.5}$$

The above equation indicates that the two-dimensional vector field given by $\tilde{v}$ and $\tilde{w}$ is divergence-less. The distribution of $\tilde{v}$ can be thus determined if $\tilde{w}$ is known (or *vice versa*), and the two form a single circulatory pattern. Such a cross-sectional circulatory motion is typical of secondary motions (see e.g. Neuhauser *et al.* 2022) and will be treated separately from the remaining velocity component $\tilde{u}$, which contains the information regarding the momentum pathways (e.g. Womack *et al.* 2022).

3.2. *Velocity spectra of the dispersive field*

In § 4, the dispersive field of the simulated flows will be inspected in real space to reveal the presence of secondary motions and their features. An additional analysis will be performed in spectral space by scrutinising the velocity spectra $\Phi_{\tilde{u}\tilde{u}}$, $\Phi_{\tilde{v}\tilde{v}}$, $\Phi_{\tilde{w}\tilde{w}}$ of the dispersive field. Velocity spectra are typically defined as the Fourier transform of the velocity correlation function (see, e.g., Davidson 2015). Such a definition cannot be used in the present case

owing to the periodicity of the dispersive field: a Fourier series is used instead. As an example, the spectrum $\Phi_{\tilde{u}\tilde{u}}$ of $\tilde{u}$ is defined as

$$\Phi_{\tilde{u}\tilde{u}} = \frac{\mathcal{F}_z\{\tilde{u}\}^\dagger \mathcal{F}_z\{\tilde{u}\}}{\Delta\kappa_z}, \tag{3.6}$$

where $(\cdot)^\dagger$ indicates the conjugate of a complex number, $\Delta\kappa_z$ is the Fourier resolution in the spanwise direction and $\mathcal{F}_z\{\tilde{u}\}$ indicates the coefficients of the Fourier series of $\tilde{u}$. These are defined as

$$\mathcal{F}_z\{\tilde{u}\}(t, y, \kappa_z) = \frac{1}{\Lambda_s} \int_0^{\Lambda_s} \tilde{u}(t, y, \zeta) \, e^{-i\kappa_z \zeta} \, \mathrm{d}\zeta \tag{3.7}$$

where i is the imaginary unit and κ_z the spanwise wavenumber. Owing to Parseval's theorem, the spectrum of $\tilde{u}$ can be related to the spanwise average of its energy:

$$\sum_{\kappa_z=-\infty}^{+\infty} \Delta\kappa_z \Phi_{\tilde{u}\tilde{u}}(t, y, \kappa_z) = \frac{1}{\Lambda_s} \int_0^{\Lambda_s} \tilde{u}^2(t, y, \zeta) \, \mathrm{d}\zeta = \langle\tilde{u}^2\rangle_z \tag{3.8}$$

The above equation justifies the common interpretation of the spectrum as the contribution of motions of wavelength $\lambda_z = 2\pi/\kappa_z$ to the energy of the flow.

3.3. *Triple-decomposed momentum and velocity budgets*

Additionally to the spectra, the energy budget of the streamwise dispersive velocity component $\tilde{u}$ will be analysed at a steady state in §4. For completeness, and to shed light on the way energy is redistributed between the mean, dispersive and fluctuation fields, each of the corresponding budget equations will be presented in the following discussion (including equations that will not be further discussed in the paper). These budget equations can be easily obtained starting from the Reynolds-averaged momentum budget and from the budget equation of the Reynolds stress tensor (see, e.g., Davidson 2015):

$$\frac{\partial \langle u_i \rangle}{\partial t} + \langle u_k \rangle \frac{\partial}{\partial x_k} \langle u_i \rangle + \frac{1}{\rho} \frac{\partial \langle P \rangle}{\partial x_i} = \nu \nabla^2 \langle u_i \rangle - \frac{\partial}{\partial x_k} \langle u_i' u_k' \rangle. \tag{3.9}$$

$$\begin{aligned}
\frac{\partial \langle u_i' u_j' \rangle}{\partial t} + \langle u_k \rangle \frac{\partial}{\partial x_k} \langle u_i' u_j' \rangle = &- \langle u_i' u_k' \rangle \frac{\partial \langle u_j \rangle}{\partial x_k} - \langle u_j' u_k' \rangle \frac{\partial \langle u_i \rangle}{\partial x_k} \\
&- \frac{\partial}{\partial x_k} \langle u_i' u_j' u_k' \rangle - \frac{\partial}{\partial x_i} \left\langle u_j' \frac{P'}{\rho} \right\rangle - \frac{\partial}{\partial x_j} \left\langle u_i' \frac{P'}{\rho} \right\rangle \\
&+ \left\langle \frac{P'}{\rho} \left(\frac{\partial u_i'}{\partial x_j} + \frac{\partial u_j'}{\partial x_i} \right) \right\rangle \\
&+ \nu \nabla^2 \langle u_i' u_j' \rangle - 2\nu \left\langle \frac{\partial u_i'}{\partial x_k} \frac{\partial u_j'}{\partial x_k} \right\rangle.
\end{aligned} \tag{3.10}$$

The above equations are usually derived by time-averaging, whereas the present work resorts to averaging in the streamwise direction, over multiple repetitions of a simulation and over multiple phases of a periodic domain. Nevertheless, it is trivially shown that the above equations are valid regardless of how averaging is performed as long as the averaging operator fulfils the following properties (as it does in this case):

$$\langle f' \rangle = 0; \quad \langle \langle f \rangle \rangle = \langle f \rangle; \quad \langle \langle f \rangle f' \rangle = \langle f \rangle \langle f' \rangle, \tag{3.11}$$

where f indicates a generic random function. Equation (3.9) is only valid for the expected velocity field $\langle \boldsymbol{u} \rangle$; leveraging the fact that the triple decomposition is a particular case of the Reynolds one, a budget equation for the ith component U_i of the mean field can be obtained by substituting (3.1) in (3.9) and taking a spanwise average:

$$\frac{\partial U_i}{\partial t} + U_k \frac{\partial U_i}{\partial x_k} + \frac{1}{\rho} \frac{\partial \langle P \rangle_z}{\partial x_i} = \nu \nabla^2 U_i - \frac{\partial}{\partial x_k} \langle \tilde{u}_i \tilde{u}_k \rangle_z - \frac{\partial}{\partial x_k} \langle u_i' u_k' \rangle_z. \tag{3.12}$$

The above equation resembles the Reynolds-averaged Navier–Stokes momentum equation (3.9), except that an additional term appears. Not only does the mean field feel the presence of turbulence through the Reynolds stress $\langle u_i' u_k' \rangle_z$, but it is also influenced by the dispersive field through the dispersive stress $\langle \tilde{u}_i \tilde{u}_k \rangle_z$. Notice, moreover, that (2.4), which describes the time-evolution of the bulk velocity, can be obtained by integrating (3.12) over the flow domain. By once again substituting (3.1) in (3.9) and by subtracting (3.12), one obtains a balance equation for the dispersive momentum:

$$\frac{\partial \tilde{u}_i}{\partial t} + (U_k + \tilde{u}_k) \frac{\partial \tilde{u}_i}{\partial x_k} + \frac{1}{\rho} \frac{\partial \tilde{p}}{\partial x_i} = \nu \nabla^2 \tilde{u}_i \underbrace{- \tilde{u}_k \frac{\partial U_i}{\partial x_k}}_{V4} + \frac{\partial}{\partial x_k} \langle \tilde{u}_i \tilde{u}_k \rangle_z \tag{3.13}$$
$$- \frac{\partial}{\partial x_k} \left(\langle u_i' u_k' \rangle - \langle u_i' u_k' \rangle_z \right),$$

where $\tilde{u}_i$ indicates the ith component of $\boldsymbol{u}_d$. Notice that (3.12) and (3.13) are of general validity (symmetries and simplifications due to the geometry have not been considered yet). Starting from the momentum budgets (3.12) and (3.13), energy budgets are trivially obtained by multiplication with U_i and $\tilde{u}_i$, respectively, and by performing a subsequent spanwise average. Additionally, an energy budget for the fluctuation field can be obtained by substituting (3.1) in (3.10) and by spanwise-averaging. After rearranging some terms, one obtains

$$\frac{\partial}{\partial t} \frac{U_i^2}{2} + U_k \frac{\partial}{\partial x_k} \frac{U_i^2}{2} = \nu \nabla^2 \frac{U_i^2}{2} - \nu \left(\frac{\partial U_i}{\partial x_k} \frac{\partial U_i}{\partial x_k} \right) - \frac{U_i}{\rho} \frac{\partial \langle P \rangle_z}{\partial x_i} \tag{3.14}$$
$$+ \underbrace{\langle \tilde{u}_i \tilde{u}_k \rangle_z \frac{\partial U_i}{\partial x_k} + \langle u_i' u_k' \rangle_z \frac{\partial U_i}{\partial x_k}}_{M5}$$
$$- \frac{\partial}{\partial x_k} \left[U_i \left(\langle \tilde{u}_i \tilde{u}_k \rangle_z + \langle u_i' u_k' \rangle_z \right) \right],$$

$$\frac{\partial}{\partial t} \frac{\langle \tilde{u}_i^2 \rangle_z}{2} + \underbrace{\frac{\partial}{\partial x_k} \left\langle (U_k + \tilde{u}_k) \frac{\tilde{u}_i^2}{2} \right\rangle_z}_{D1} = \underbrace{\nu \nabla^2 \frac{\langle \tilde{u}_i^2 \rangle_z}{2}}_{D2} \underbrace{- \nu \left\langle \frac{\partial \tilde{u}_i}{\partial x_k} \frac{\partial \tilde{u}_i}{\partial x_k} \right\rangle_z}_{D3} \underbrace{- \left\langle \frac{\tilde{u}_i}{\rho} \frac{\partial \tilde{P}}{\partial x_i} \right\rangle_z}_{D4} \tag{3.15}$$
$$\underbrace{- \langle \tilde{u}_i \tilde{u}_k \rangle_z \frac{\partial U_i}{\partial x_k}}_{D5} + \underbrace{\left\langle \langle u_i' u_k' \rangle \frac{\partial \tilde{u}_i}{\partial x_k} \right\rangle_z}_{D6}$$
$$\underbrace{- \frac{\partial}{\partial x_k} \langle \tilde{u}_i \langle u_i' u_k' \rangle \rangle_z}_{D7},$$

$$\frac{\partial}{\partial t}\frac{\langle u_i' u_i'\rangle_z}{2} + \frac{\partial}{\partial x_k}\left\langle (U_k + \tilde{u}_k)\frac{\langle u_i' u_i'\rangle}{2}\right\rangle_z = + \nu\nabla^2\frac{\langle u_i' u_i'\rangle_z}{2} - \nu\left\langle\frac{\partial u_i'}{\partial x_k}\frac{\partial u_i'}{\partial x_k}\right\rangle_z$$

$$- \langle u_i' u_k'\rangle_z\frac{\partial U_i}{\partial x_k} - \underbrace{\left\langle\langle u_i' u_k'\rangle\frac{\partial\tilde{u}_i}{\partial x_k}\right\rangle_z}_{\text{F6}}$$

$$- \frac{1}{2}\frac{\partial}{\partial x_k}\langle u_i' u_i' u_k'\rangle_z - \frac{\partial}{\partial x_i}\left\langle\frac{u_i'}{\rho}P'\right\rangle_z. \quad (3.16)$$

The above equations were also found by Reynolds & Hussain (1972) using a slightly different averaging technique. Consider the equation for the dispersive kinetic energy (3.15). The dispersive kinetic energy gets transported by both the mean and the dispersive fields (term D1); a pressure term appears in the equation (D4), as well as the usual viscous diffusion (D2) and dissipation (D3) terms. The former indicates that viscosity tends to smear the dispersive energy out over time, whereas the latter represents the power lost to viscous forces. The two remaining equations ((3.14) and (3.16)) all share analogous transport, pressure and viscous terms; the only difference is that the mean kinetic energy U_i^2 is only transported by the mean field U_i, and not by the dispersive one $\tilde{u}_i$.

Most importantly, the above equations shed a light on how the mean, dispersive and fluctuation fields exchange energy. For instance, the dispersive stress term D5 appears both in the balance of dispersive energy (3.15) and in the balance of mean energy (3.14) (term M5) with opposite sign: it thus represents an exchange of power between the mean and the dispersive fields. Similarly, term D6 represents an exchange of power between the dispersive and fluctuation fields, as it appears both in the dispersive balance and in the fluctuation one (3.16) (term F6) with opposite sign. To sum up, the dispersive stresses enable the exchange of energy between the mean and the dispersive fields, whereas the Reynolds stresses allow the exchange of energy between the dispersive and the fluctuation field (and additionally between the mean and the fluctuation field, as is usual; see (3.14) and (3.16)).

In § 4, only the energy budget of the streamwise dispersive energy $\tilde{u}^2$ will be analysed; indeed, the quantities involved in the budgets of the two remaining components $\tilde{v}^2$ and $\tilde{w}^2$ are too small compared with the fluctuations to be captured with a satisfactory signal-to-noise ratio. Such a $\tilde{u}^2$-budget can be obtained in a similar way to (3.15), but without averaging in the spanwise direction; after considering all the simplifications and symmetries due to the present geometry, the budget reads

$$\frac{\partial}{\partial t}\frac{\tilde{u}^2}{2} + \underbrace{\left(\tilde{v}\frac{\partial}{\partial y} + \tilde{w}\frac{\partial}{\partial\zeta}\right)\frac{\tilde{u}^2}{2}}_{\mathcal{T}_a} = \underbrace{\nu\nabla^2\frac{\tilde{u}^2}{2} - \nu\left(\frac{\partial\tilde{u}}{\partial y}\frac{\partial\tilde{u}}{\partial y} + \frac{\partial\tilde{u}}{\partial\zeta}\frac{\partial\tilde{u}}{\partial\zeta}\right)}_{\mathcal{V}} + \underbrace{\tilde{u}\frac{\partial}{\partial y}\langle\tilde{u}\tilde{v}\rangle_z}_{\mathcal{T}_c}$$

$$\underbrace{-\tilde{u}\tilde{v}\frac{\partial U}{\partial y}}_{\mathcal{P}} \underbrace{-\tilde{u}\frac{\partial}{\partial y}\left(\langle u'v'\rangle - \langle u'v'\rangle_z\right)}_{\mathcal{T}_{uv}} \underbrace{-\tilde{u}\frac{\partial}{\partial\zeta}\langle u'w'\rangle}_{\mathcal{T}_{uw}}. \quad (3.17)$$

An additional term appears here with respect to (3.15) – that is, $\mathcal{T}_c$. This term integrates to zero when spanwise-averaged, both explaining its absence from (3.15) and indicating that the term only spatially redistributes $\tilde{u}$-energy. The remaining terms all have a correspondent in (3.15). Notice that here, both the viscous diffusion (D2 in (3.15)) and the viscous dissipation (D3) are grouped in a single term $\mathcal{V}$. The terms $\mathcal{T}_{uv}$ and $\mathcal{T}_{uw}$ quantify the work done by the Reynolds stresses on the dispersive velocity $\tilde{u}$. Such work

was rewritten in (3.15) as two separate terms (D6 and D7), of which one (D6) corresponds to a power exchange with the fluctuation field, and the other (D7) can be easily shown to turn zero for the $\tilde{u}$ component when integrated over the flow domain (notice that the same does not hold for the w component owing to the slip length boundary condition). That is, term D7 only yields a spatial redistribution of $\tilde{u}$-energy.

Finally, the $\mathcal{P}$ term of (3.17) is of particular interest for the results of this paper. We refer to such a term as *dispersive production* owing to its similarity to the canonical turbulence production term in a channel flow (Davidson 2015). Such a term corresponds to the D5 term in (3.15), and it thus represents an energy exchange with the mean field. The term accounts for the work done by the momentum flux V4 in (3.13) on the velocity $\tilde{u}$. The momentum flux is better discussed by considering the balance of streamwise momentum and by applying all simplifications due to the geometry:

$$-\tilde{v}\frac{\partial U}{\partial y}. \tag{3.18}$$

It is clear from (3.18) that the discussed momentum flux originates from $\tilde{v}$ transporting the mean field U. In other words, the circulatory dispersive $\tilde{v}$-$\tilde{w}$ motions do not directly provide energy to the streamwise component $\tilde{u}$, but still passively enable the transfer of energy from the mean flow to $\tilde{u}$ by transporting U-momentum. A more intuitive explanation of how the $\tilde{u}$ field is indirectly produced by the circulatory motions (under certain circumstances) will be provided in § 4 using flow visualisations as an example.

3.4. *Time scale for the decay of secondary motions; volume and plane averages*

In § 5, the time needed by secondary motions to decay will be measured as per the objective of this study. Before doing so, such a time scale needs to be defined. Defining a time scale for the decay of turbulent eddies is a largely subjective process. For instance, Flores & Jiménez (2010) found that the log-layer of turbulent flows in a restricted simulation box bursts quasiperiodically, and linked the estimated period to the life span of log-layer eddies. LeHew *et al.* (2013) and Lozano-Durán & Jiménez (2014), instead, resorted to identifying turbulent coherent structures and tracking them in time; their lifespan is given by the distance in time between their first and last identification. In our case, no sophisticated strategy is needed to track the secondary motions, as their spatial position is fixed and their features are satisfactorily captured by the dispersive velocity field $\boldsymbol{u}_d$ (as will be discussed in § 4). We thus define some energy measure $e(t) \geqslant 0$ using the dispersive velocity and track it in time; the energy will start from a value $e(0)$ seen at the steady state and then decline to zero for $t \to \infty$ as the secondary motions decay. The time scale T for the decay can then be defined as the time required for most of the energy to vanish; more precisely, as the minimum value of t after which the energy e never exceeds a threshold ϵ:

$$T \mid e(T) = \epsilon, \ e(T + \Delta t) < \epsilon \ \ \forall \ \ \Delta t > 0. \tag{3.19}$$

A graphical representation of the above definition is provided in figure 2; in the figure, the generic energy measure e is replaced by the volume-averaged quantity I_u (defined in the next paragraph). The threshold ϵ is set to 15 % of the initial value $e(0)$ for multiple reasons. First, having a large threshold is beneficial for the signal-to-noise ratio: the smaller the measured value of e, the greater its relative statistical uncertainty. It is moreover desirable to let the value of the threshold depend on the initial condition: secondary motions with different values of Λ_s/h hold different amounts of energy at a steady state (Wangsawijaya & Hutchins 2022). It would not be sensible, then, to compare the time to decay of secondary motions of different sizes as measured by a fixed ϵ: every secondary
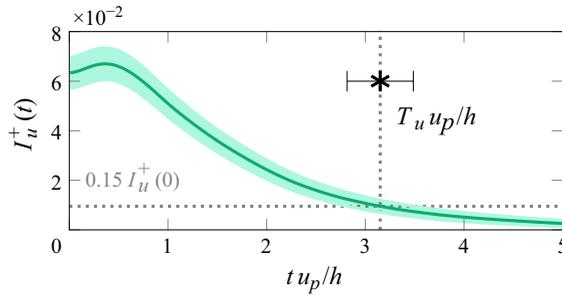
Figure 2. Graphical representation of the definition of the time T_u needed for the pattern of streamwise dispersive velocity to decay. Such a time scale is defined by applying (3.19) to the volume-averaged energy I_u. The dark green line represents the time evolution of I_u; the lighter green area its 95 % confidence interval (as per § 3.5). Similarly, a marker with an error bar is used to indicate T_u and its 95 % confidence interval (see, once again, § 3.5). The horizontal dotted line indicates the threshold value $\epsilon = 0.15\, I_u(0)$ used to define T_u. Data at $Re_\tau = 500$, $\Lambda_s/h = 2$.

motion starts from a different initial energy value. Instead, by letting $\epsilon = 15\,\%\, e(0)$, the inverse $1/T$ of the time scale measures some sort of generalised decay rate ($1/T$ would exactly be a multiple of the decay rate in the case of an exponential decay).

It remains to be specified which energy measure is used to calculate the time scale. In this respect, two different approaches will be pursued. To begin with, the energy of the dispersive field will be volume-averaged to yield two values I_u and I_{vw} for the streamwise and circulatory patterns, respectively:

$$I_u(t) = \frac{1}{2h} \int_0^{2h} \frac{1}{2}\langle \tilde{u}^2 \rangle_z \, \mathrm{d}y, \tag{3.20}$$

$$I_{vw}(t) = \frac{1}{2h} \int_0^{2h} \frac{1}{2}\langle \tilde{v}^2 + \tilde{w}^2 \rangle_z \, \mathrm{d}y. \tag{3.21}$$

By applying the (3.19) to the above quantities, the time scales T_u and T_{vw} for the streamwise pattern and for the circulatory motions are obtained. The streamwise pattern and the circulatory motions are indeed two separate features of the dispersive fields as discussed in § 3.1; they will be thus treated separately.

The above approach defines two scalar quantities – I_u and I_{vw} – which can be easily tracked in time; their interpretation is also straightforward, as they represent the cumulative amount of energy held by secondary motions. However, such an approach is unable to capture the spatial complexity of the secondary motions. To recover some of it, for instance, one might resort to averaging the dispersive energy on wall-parallel planes. As an example, the plane-average i_u of the streamwise energy is defined as follows:

$$i_u(t, y) = \frac{1}{2}\langle \tilde{u}^2 \rangle_z. \tag{3.22}$$

Doing so, wall-normal energy variations can be investigated. Bear in mind (see (3.8)) that the value of i_u seen at some wall-normal position y is equal to the sum of all the energy contributions (as measured by the spectrum $\Phi_{\tilde{u}\tilde{u}}$) of the Fourier modes $\mathcal{F}_z\{\tilde{u}\}$ at that same position y. Leveraging this property, one can also apply (3.19) of the time scale to the dispersive spectrum $\Phi_{\tilde{u}\tilde{u}}$. The resulting time scale describes the life time of motions of given spanwise wavelength $\lambda_z = 2\pi/\kappa_z$ at a given wall-normal height y.

3.5. *Estimation of the dispersive field and uncertainty quantification*

As previously explained, expected values are indicated by $\langle \cdot \rangle$ throughout the present article. With the exception of this section, the same symbol is also used to indicate the estimates of such expected values as computed using the present data. The estimates deviate from the actual expected values as they are calculated on a sample of finite size; in other words, the estimates are affected by statistical uncertainty. It is assumed that statistical uncertainty dominates other sources of error (such as discretisation and round-off error, or the error introduced by the limited domain size), so that the overall uncertainty on the estimated statistics is given by the statistical uncertainty alone. This section deals with the quantification of such statistical uncertainty.

In particular, the uncertainty on the dispersive velocity field is of interest – as its values are referenced in the main results of this study. For the sake of clarity, the estimator of the dispersive velocity will be indicated by $\breve{u}_i$, whereas its exact (theoretical) value will be $\tilde{u}_i$ as usual:

$$\tilde{u}_i \approx \breve{u}_i. \tag{3.23}$$

Here, the subscript i indicates the component, so that $(\tilde{u}_1, \tilde{u}_2, \tilde{u}_3) = (\tilde{u}, \tilde{v}, \tilde{w})$. The dispersive field is estimated through a streamwise-, phase- and ensemble-average; such operation can be reinterpreted as the arithmetic mean of a set of intermediate averages $\overline{u}_{i,k}^{x\Delta}$:

$$\breve{u}_i = \frac{1}{N_s} \sum_{k=1}^{N_s} \underbrace{\frac{\Lambda_s}{L_z} \int_0^{L_z} \Delta_z(z + \zeta) \left(\frac{1}{L_x} \int_0^{L_x} u_{i,k} - \langle u_{i,k} \rangle_z \, \mathrm{d}x \right) \mathrm{d}z}_{\overline{u}_{i,k}^{x\Delta}}, \tag{3.24}$$

where the index k refers to one of the N_s repetitions of a given simulation and Δ_z is a Dirac comb function used for the computation of the phase-average; by indicating Dirac's delta distribution as δ,

$$\Delta_z = \sum_{j=1}^{L_z/\Lambda_s - 1} \delta \left(z + j\Lambda_s \right). \tag{3.25}$$

The N_s values of $\overline{u}_{i,k}^{x\Delta}$ computed from the many repetitions of each simulation should be reasonably uncorrelated owing to the discussion of §2.1. In light of the central limit theorem (Billingsley 1995), then, the probability distribution function of $\breve{u}_i$ can be modelled by a normal distribution (indicated by $\mathcal{N}$) with mean $\tilde{u}_i$; its standard deviation $\breve{\sigma}_i$ can be estimated from the standard deviation $\overline{\sigma}_i^{x\Delta}$ of the set of values of $\overline{u}_{i,k}^{x\Delta}$ (which, in turn, is directly computed):

$$\breve{u}_i \sim \mathcal{N} \left(\tilde{u}_i, \breve{\sigma}_i \right), \tag{3.26}$$

$$\breve{\sigma}_i = \frac{\overline{\sigma}_i^{x\Delta}}{\sqrt{N_s}}. \tag{3.27}$$

Note that, in the context of the present discussion, the cross-correlation between different components of $\breve{u}_i$ is neglected; this simplification does not affect the estimates of the uncertainty on I_u. Owing to the above discussion, the 95 % confidence interval for the estimate of $\tilde{u}_i$ is given by

$$\tilde{u}_i = \breve{u}_i \pm \mathcal{E}\{\tilde{u}_i\} = \breve{u}_i \pm 2\breve{\sigma}_i. \tag{3.28}$$

Hence, the uncertainty $\mathcal{E}\{\tilde{u}_i\}$ can be propagated, as an example, to the energy $\tilde{u}^2/2$ of the streamwise field:

$$\mathcal{E}\left\{\frac{\tilde{u}^2}{2}\right\} \approx \sqrt{\left(\frac{\mathrm{d}\tilde{u}^2/2}{\mathrm{d}\tilde{u}}\right)_{\check{u}}^2 (\mathcal{E}\{\tilde{u}\})^2} = |\check{u}|\,\mathcal{E}\{\tilde{u}\}. \tag{3.29}$$

Next, the uncertainty is propagated to the estimate of I_u. In theory, this would require modelling the correlation between the values of $\tilde{u}^2/2$ at different spatial position. However, a pessimistic estimate of the uncertainty on I_u can be found as follows. It is assumed that extreme events (meaning events for which $(\overline{u}^{x\Delta})^2/2$ falls outside of the 95 % confidence interval for $\tilde{u}^2/2$) happen simultaneously at all spatial positions. In other words, given that an extreme event occurs at some spatial position, one is certain to observe an extreme event at any other spatial position. This is a pessimistic assumption: likely, extreme events are confined in space and do not involve the whole flow domain. However, such an assumption might account for large eddies possibly triggering extended coherent regions of extreme events. In light of the above assumption, the error on I_u is estimated as

$$\mathcal{E}\{I_u\} \approx \frac{1}{2h}\int_0^{2h}\left\langle\mathcal{E}\left\{\frac{\tilde{u}^2}{2}\right\}\right\rangle_z\,\mathrm{d}y. \tag{3.30}$$

Similar considerations can be leveraged to estimate the uncertainty affecting I_{vw} and $\Phi_{\tilde{u}\tilde{u}}$.

Finally, the uncertainty can be propagated to the time scale T_u defined by I_u. To do so, the (estimated) value of the time derivative $I_{u,t}$ of I_u at the time T_u is used:

$$\mathcal{E}\{T_u\} \approx \sqrt{\frac{1}{I_{u,t}^2(T_u)}}\,\mathcal{E}\{I_u\}. \tag{3.31}$$

Once again, a similar procedure can be used to quantify the uncertainty on the time scales defined by I_{vw} and $\Phi_{\tilde{u}\tilde{u}}$.

4. Steady-state secondary motions

In this section, we analyse the dispersive velocity field (as defined in § 2) at the initial steady state. We argue that the main consequence of the presence of strip-type roughness is the existence of a non-zero dispersive velocity field. Later on, in light of this analysis, the dispersive velocity field will be tracked in time as the secondary motions decay.

The dispersive velocity field is linked to an easily identifiable and isolable feature of the velocity spectra of the investigated flows over heterogeneous roughness. As an example, we compare the two-dimensional streamwise velocity spectra of two flows at $Re_\tau = 500$, one of which runs between smooth walls (figure 3a) whereas the other (figure 3b) runs over a roughness pattern ($\Lambda_s/h = 1$). This combination of parameters has been chosen to best highlight the observed behaviour and is representative of the remaining cases. The bar below each panel shows the $\kappa_x = 0$ mode (where κ_x is the Fourier wavenumber in the streamwise direction; κ_z is that in the spanwise direction), which would otherwise not be visible owing to the logarithmic scale. The $\kappa_x = 0$ mode is premultiplied with the Fourier resolution $\Delta\kappa_x = 2\pi/L_x$ of the spatial grid. The spectrum is evaluated in proximity of the wall ($y^+ = 10$), as, according to the attached eddy model of turbulence (Marusic & Monty 2019), most scales of motion are observable at this wall-normal location. Further away from the wall, only the largest scales would be visible. This heuristic is confirmed by the spectra of the isolated dispersive motion, later shown in figure 6. Notice that no decomposition is used (unless explicitly stated), so that the spectra include both features linked to velocity fluctuations and to the dispersive velocity.
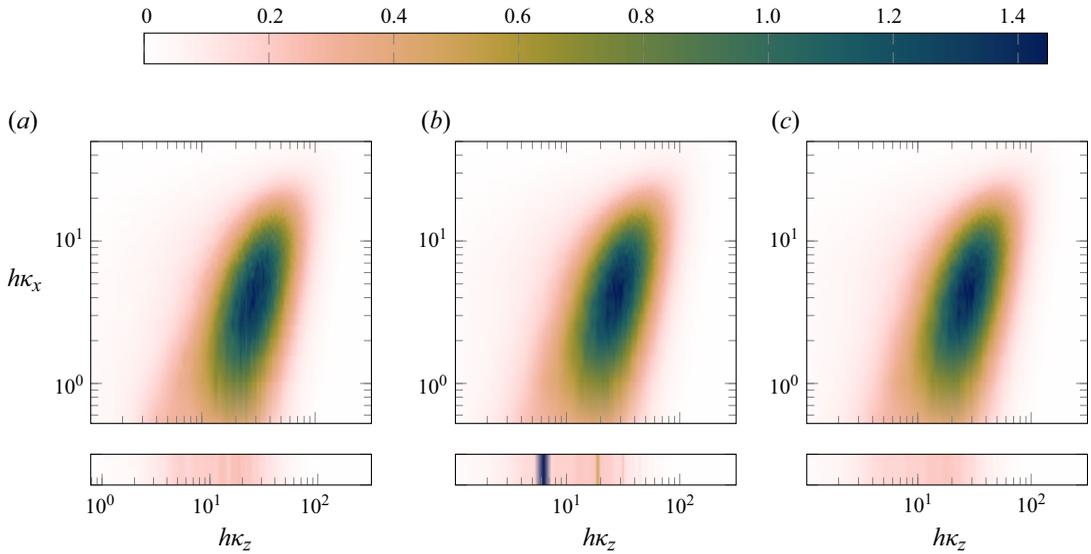
Figure 3. Inner-scaled premultiplied two-dimensional velocity spectra at $y^+ = 10$ for steady-state simulations. The bar below each panel represents the mode $\kappa_x = 0$, which would otherwise not be visible due to the logarithmic scale. (*a*) Premultiplied spectrum $\kappa_x^+ \kappa_z^+ \phi_{uu}^+$ of the streamwise fluctuations; $Re_\tau = 500$, smooth walls. (*b*) Premultiplied spectrum of the full streamwise velocity signal (including both the dispersive velocity and fluctuations); $Re_\tau = 500$, $\Lambda_s/h = 1$. (*c*) Premultiplied spectrum $\kappa_x^+ \kappa_z^+ \phi_{uu}^+$ of the streamwise fluctuations; $Re_\tau = 500$, $\Lambda_s/h = 1$ (same as panel *b*, but the contribution of the dispersive velocity is removed).

All panels of figure 3 share the same qualitative spectral peak typical of turbulent fluctuations; in agreement with the attached-eddy hypothesis, most of the energy is seen on (κ_x, κ_z)-modes of roughly constant aspect ratio, meaning that motions that are large in the x-direction also tend to be large in z. The dominant feature that differentiates the (*a*) smooth and the (*b*) rough spectra is the occurrence of a banded energy pattern at $\kappa_x = 0$ in panel (*b*). This banded pattern is associated with the dispersive velocity: by removing the latter in panel (*c*), the energy bands are also eliminated so that the remaning spectrum can be hardly distinguished from that of the smooth case. In other words, the dispersive average captures the main spectral feature differentiating a flow over a smooth wall from that over strip-type roughness.

Nevertheless, further and yet less apparent differences arise between smooth and rough spectra; a separate analysis (not shown for brevity) shows for instance that the spectral peak associated with turbulent fluctuations gets closer to the wall in the presence of a roughness pattern. This is expected: consistently with the protrusion height theory of Luchini *et al.* (1991), using a sliplength to model roughness (as we do) aims at pulling turbulence fluctuations towards the wall to locally increase the wall shear stress (Gatti *et al.* 2018; Neuhauser *et al.* 2022). As for the meandering of secondary motions (Wangsawijaya *et al.* 2020), we do not observe any spectral feature that can be clearly linked to it. Meandering would manifest itself as energy content for $\kappa_x \neq 0$ at the same κ_z values of the banded energy pattern associated with the dispersive velocity. The lack of such features is perhaps a consequence of the relatively low Reynolds number; most importantly, meandering is best observed at larger values of y^+ than that used in figure 3 (Wangsawijaya *et al.* 2020).

Having found that the dispersive velocity isolates a distinct feature of the turbulent spectra, we proceed to inspect it both in real and Fourier space. Figure 4 shows the dispersive velocity field for all available values of Λ_s/h at $Re_\tau = 500$. The averaged

1007 A19-16
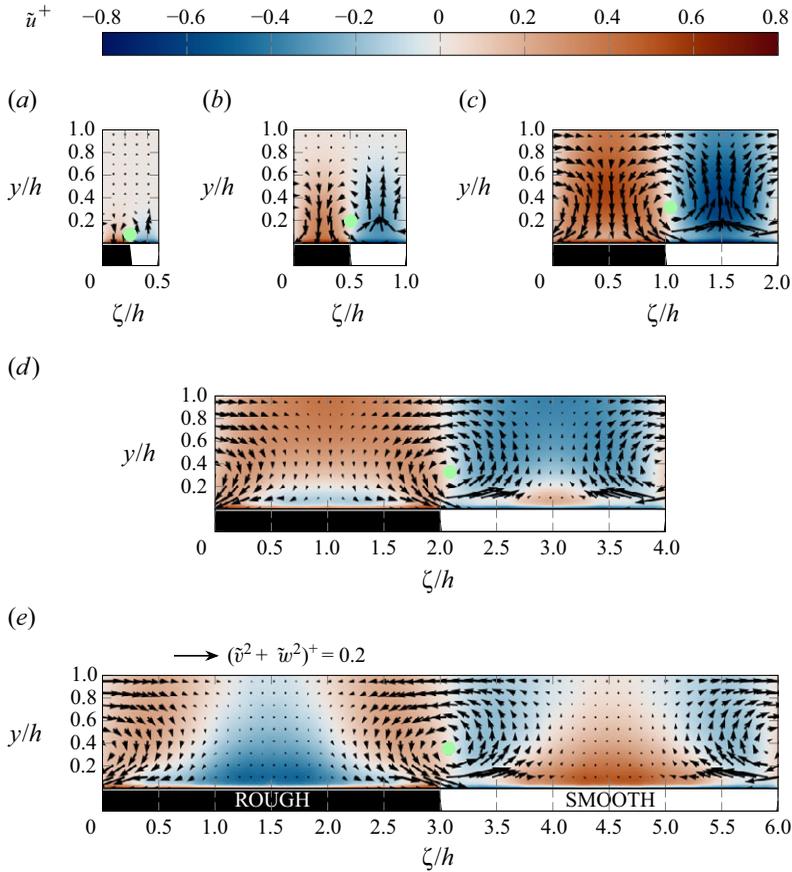
Figure 4. Dispersive velocity field at the initial steady state ($t = 0$) divided in its streamwise $\tilde{u}^+$ (colour) and circulatory $\tilde{v}^+$-$\tilde{w}^+$ (arrows) patterns; all data at $Re_\tau = 500$: (a) $\Lambda_s/h = 0.5$; (b) $\Lambda_s/h = 1$; (c) $\Lambda_s/h = 2$; (d) $\Lambda_s/h = 4$; (e) $\Lambda_s/h = 6$. The arrow length is proportional to the magnitude of the represented vector; the scale is graphically represented above panel (e) and is consistent across all panels. Below each panel, we indicate whether the wall at that spanwise position is rough (black) or smooth (white). A green dot marks the position of the vortex centre as defined later in § 5.1.

flow fields at $Re_\tau = 180$ (not shown for brevity) return a similar picture. Similarly to other studies concerning secondary motions (Chung *et al.* 2018) and flow over multi-scale roughness (Barros & Christensen 2014; Womack *et al.* 2022), these visualisations reveal the presence of high- and low-momentum pathways flanked by circulatory motions. A similar flow topology is also seen in the conditional views of the fluctuation field linked to VLSMs (Hutchins & Marusic 2007b). For low strip widths ($\Lambda_s/h \lesssim 2$ roughly), regions of downwash ($\tilde{v} < 0$, or sweep events) coincide with regions of high streamwise momentum, and *vice versa* for ejection events ($\tilde{v} > 0$). Secondary motions are confined to a region close to the wall for $\Lambda_s/h = 0.5$; they grow taller as the strip width is increased (up to $\Lambda_s/h \approx 2$). For $\Lambda_s/h = 2$, the secondary motions fill the entire channel half-height; under such conditions, high absolute values of streamwise dispersive momentum (regions of darker colour in figure 4) are seen at two separate wall-normal positions. One is located in the immediate proximity of the wall; here, the spanwise distribution of $\tilde{u}$ is well described by a square wave. The velocity distribution in this region is a good approximant of the distribution of wall shear stress, which is in turn affected by the square-wave spanwise

roughness pattern we impose. Further away from the wall, the $\tilde{u}$-distribution becomes sinuisoidal in the spanwise direction; a second region of intense momentum appears around $y/h \approx 0.4$ ($y^+ \approx 200$).

As the strip width is further increased (roughly $\Lambda_s/h > 2$), the circulatory cross-plane motions shown by the v-w vector field are progressively confined to the roughness transitions – that is, the interfaces between adjacent rough and smooth strips. As previously observed for lower strip widths, $\tilde{u}$ and $\tilde{v}$ are anti-correlated where these intense circulatory motions are present. At the centre of each strip, instead, the $\tilde{u}$-velocity approaches local equilibrium with the wall (Chung *et al.* 2018; Neuhauser *et al.* 2022). The expected square-wave pattern of $\tilde{u}$ is seen at the wall; moving away from it, $\tilde{u}$ changes in sign at the centre of each strip. For $\Lambda_s/h = 4$ (figure 4*d*), this region of reversed sign is bounded in the wall-normal direction; for $\Lambda_s/h = 6$ (figure 4*e*), instead, it reaches the channel centreline.

We explain the observed reversal of the sign of $\tilde{u}$ as follows. Consider figure 4(*e*); the circulatory motions are confined to roughness transitions, whereas the flow above the centre of each strip is distant enough from the roughness transitions (and from the secondary motions) to not feel their effects. Although the wall-normal profile of the $U^+ + \tilde{u}^+$ velocity in the middle of each strip does not match that observed over homogeneous roughness or a homogeneous smooth wall, re-scaling $U + \tilde{u}$ with the local friction velocity makes it collapse on the homogeneous data (we were able to replicate this result on the present data; see Neuhauser *et al.* 2022). We say that the $U + \tilde{u}$ profile at the centre of the strips is at equilibrium with the local surface condition. Similar observations were also put forward by Chung *et al.* (2018); notice that the authors show visualisations of the $U + \tilde{u}$ field, whereas figure 4 shows the distribution of $\tilde{u}$ alone. Under homogeneous conditions, roughness is typically associated with a drag increase (if the flow rate is kept constant) or a reduction of the flow rate (if the pressure gradient is kept constant) with respect to a flow over an homogeneous smooth wall. If a slip length is used to model the roughness (as is done here), the drag increase at constant flow rate is seen as an increased wall shear stress (in physical terms), which can be exactly calculated as the position of the wall is clearly defined (the same does not hold true for real-life roughness, see e.g. Frohnapfel *et al.* 2024). Unlike the homogeneous case, the present heterogeneous set-up allows to contemporarily observe both the increase in wall shear stress (in spite of the constant pressure gradient) and the decrease in flow rate. Indeed, the pressure gradient only determines the spanwise-averaged value of the wall shear stress (see (2.4)); locally higher and lower (with respect to the spanwise average) values of the wall shear stress are permitted. Thus, the positive sign of the $\tilde{u}$-velocity in the thin near-wall region above rough strips reflects a slip-length-induced increase of the wall shear stress; its negative sign further away from the wall (and sufficiently far from the circulatory motions), instead, reflects the reduction of flow rate. By contrast, circulatory motions tend to induce a positive sign of $\tilde{u}$ over rough strips. The same line of reasoning can explain the features observed over smooth strips; bear in mind that $\tilde{u}$ represents a deviation of the averaged velocity from its spanwise average U, and not a deviation from some reference homogeneous profile. Notice, finally, that a similar reversal of the sign of the momentum pathways was observed by Medjnoun *et al.* (2020) when studying secondary motions induced by a variation of the wall geometry; in such a case though, the sign reversal is caused by the appearance of dominant tertiary motions and not by the segregation of secondary ones as in this case.

The sign of $\tilde{u}$ in regions where the circulatory motions are strong can be explained by a different mechanism. Both the $\tilde{u}$-$\tilde{v}$ anti-correlation and the fact that large absolute values of the streamwise momentum are seen at a certain distance from the wall in figure 4(*c*) suggest that the streamwise pattern $\tilde{u}$ is mainly generated by transport of the mean velocity field U by wall-normal motions $\tilde{v}$ through the dispersive production mechanism described
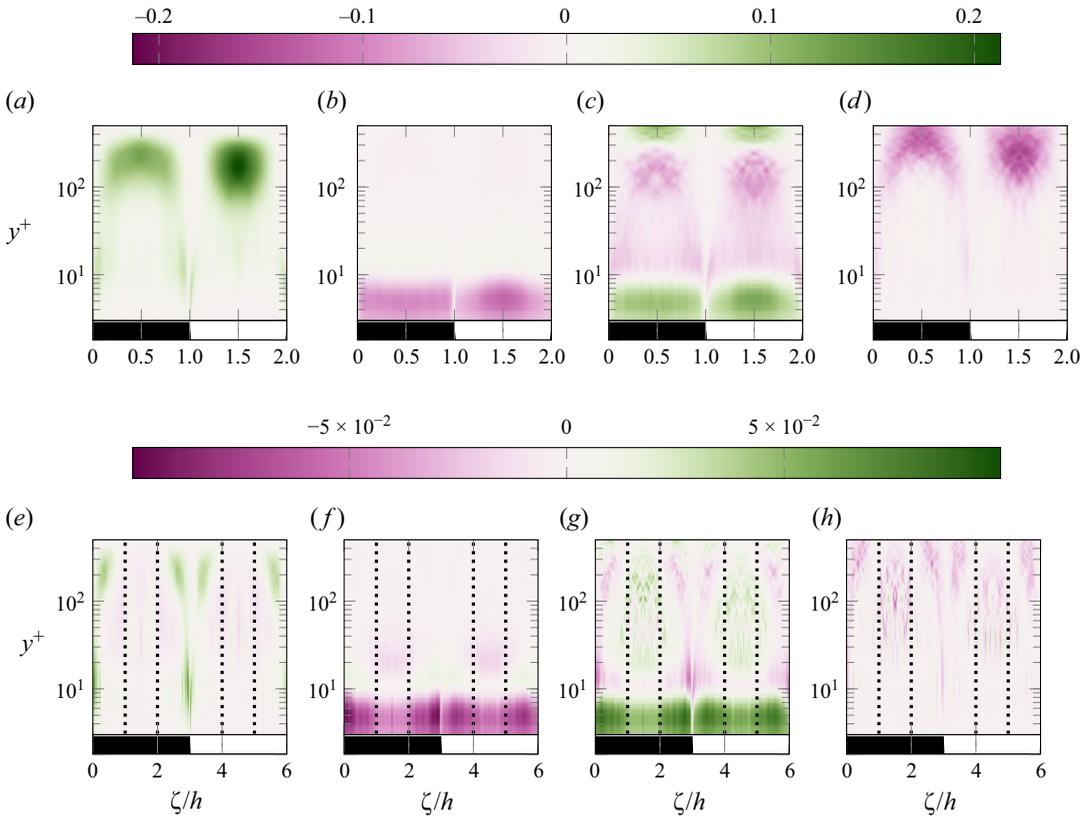
Figure 5. Inner-scaled premultiplied terms of the budget equation for the dispersive $\tilde{u}^2/2$ energy (3.17). All data at $Re_\tau = 500$, steady state. Panels (a–d) show data for $\Lambda_s/h = 2$; (a) premultiplied dispersive production $y^+\mathcal{P}^+$, (b) viscous term $y^+\mathcal{V}^+$, (c) contribution $y^+\mathcal{T}_{uv}^+$ of the $\langle u'v' \rangle$ Reynolds stress and (d) contribution $y^+\mathcal{T}_{uw}^+$ of the $\langle u'w' \rangle$ stress. Panels (e–h): same as panels (a–d) but for $\Lambda_s/h = 6$. The vertical, dotted lines in panels (e–h) roughly mark the boundary between the equilibrium and the anti-correlation regions. Please note the different scale of the horizontal axis.

at the end of § 3.3 (see (3.18)). High-speed fluid from the core of the channel (where the largest values of U are found) is transported towards the wall by a coherent downwash ($\tilde{v} < 0$) to create coherent high-momentum regions ($\tilde{u} > 0$), and *vice versa* low-speed fluid from the near-wall region is transported upwards to yield low-momentum regions. The wall-normal component $\tilde{v}$ is expected to be small in proximity of the wall, both due to the impermeability condition and to the topology of the $\tilde{v}$-$\tilde{w}$ circulatory motion. Consequently, we expect $\tilde{v}$ to be most effective at leveraging $\tilde{u}$-production at a given distance from the wall, as we observe.

To corroborate the above idea, we compute the terms of the $\tilde{u}^2$-energy budget (3.17). Such terms are shown in figure 5 at the initial steady state for two selected flow cases ($Re_\tau = 500$, $\Lambda_s/h = 2$ and $\Lambda_s/h = 6$). The advection terms $\mathcal{T}_a$ and $\mathcal{T}_c$ are not shown: although their absolute values are not exactly negligible, they are small enough to be dominated by the remaining source (or sink) terms. Positive values of each term indicate that the term is providing energy to the $\tilde{u}$ pattern, or, in other words, that the term acts to sustain the dispersive velocity. Negative values, instead, indicate that energy is being subtracted. As previously stated, while $\tilde{u}$ and $\tilde{v}$ are everywhere anti-correlated for $\Lambda_s/h = 2$, the anti-correlation region is restricted to $2h$-wide neighbourhoods of each

roughness transition for $\Lambda_s/h = 6$. We mark the borders of this region with dotted lines in panels (*e*–*h*); we refer to the remaining portion of the channel as the equilibrium region. There, the wall-normal profile of $U + \tilde{u}$ is indeed roughly at equilibrium with the local wall shear stress (see the discussion above).

The main outer-layer ($y^+ > 10$) energy donor in the anti-correlation regions of both considered flow cases is the dispersive production term (figure 5*a,e*); all remaining terms are negative, except for a minor positive contribution from $\langle u'v' \rangle$ in panel (*c*) towards the centreline. The dispersive production term is maximum around $y^+ \approx 200$; in this same region, intense values of $\tilde{u}$ were found in figure 4(*c*). This is further evidence in favour of our hypothesis that $\tilde{v}$-transport of U drives the formation of the $\tilde{u}$ pattern. It is also reminiscent of linear-transient growth analysis: the energy growth of optimally amplified modes found by studying the evolution of perturbations in linearised channel flows is driven by the same mechanism (Del Álamo & Jiménez 2006).

Both for the narrower and wider strips, the energy budget is dominated by the viscous (figure 5*b,f*) and $\langle u'v' \rangle$ (figure 5*c,g*) terms in the near-wall region ($y^+ < 10$). The former extracts energy from the intense near-wall $\tilde{u}$ pattern; most of this energy is dissipated, while part of it is returned to the flow just above $y^+ = 10$, where the term has a weak positive value (this is better observable in panel *f*). The $\langle u'v' \rangle$ stress, instead, is the main provider of energy in this region. This suggests that the formation of the near-wall $\tilde{u}$ pattern might be driven by turbulence through the Reynolds shear stress; such an interpretation is coherent with our previous findings (Andreolli *et al.* 2023), that blocking the energy exchange between small turbulent fluctuations and large ones prevents the formation of large-scaled patterns of wall shear stress. Interestingly, the $\langle u'v' \rangle$ term is also the main source of energy in the equilibrium region for the higher strip width (panel *g*), indicating that it might be responsible for driving the flow towards equilibrium. This is reasonable, as under homogeneous conditions, the mean velocity profile results from the equilibrium of viscous and $\langle u'v' \rangle$ stresses only. However, in the present context, the $\langle u'w' \rangle$ term also provides a non-negligible (negative) contribution in the equilibrium region.

Next, we inspect the dispersive velocity field in spectral space. Its spanwise spectra (defined in § 3.2) at the initial steady state are shown in figure 6 for $\Lambda_s/h = 2$, 6 and $Re_\tau = 500$. Notice that, much like the dispersive velocity, these steady-state spectra only depend on the wall-normal coordinate y and the spanwise wavenumber κ_z. The spectra better show the striped structure that was observed in figure 3; a similar pattern has also been found experimentally by Wangsawijaya & Hutchins (2022). We suggest that the striped appearance is caused by the square-wave shape of the roughness pattern we apply at the wall, whose power spectral density (shown below each panel) is also striped. It is indeed observed that most of the energy of the dispersive velocity field is found on the same Fourier modes that are excited by the roughness pattern. For both the roughness pattern and the velocity field, the first harmonic of the Fourier transform usually holds the most energy. The first harmonic is the Fourier mode whose spanwise wavelength λ_z matches the period Λ_s of the original signal; higher harmonics have a wavelength that is a fraction of such a period. For convenience, we define a harmonic number Λ_s/λ_z, such that the first harmonic has $\Lambda_s/\lambda_z = 1$, the second $\Lambda_s/\lambda_z = 2$ and so on. The harmonic number is shown at the top of each panel in figure 6.

In proximity of the wall, energy is seen on a wide range of wavelengths, reinforcing the idea that the velocity distribution there roughly takes the shape of a square wave. As a rule of thumb, energy is restricted to progressively larger Fourier modes as one moves away from the wall, this being reminiscent of the attached eddy hypothesis (see, for instance, Baars *et al.* 2017), until the velocity field is dominated by a single sinusoidal wave at the centreline. There is however a notable exception to this trend of larger Fourier
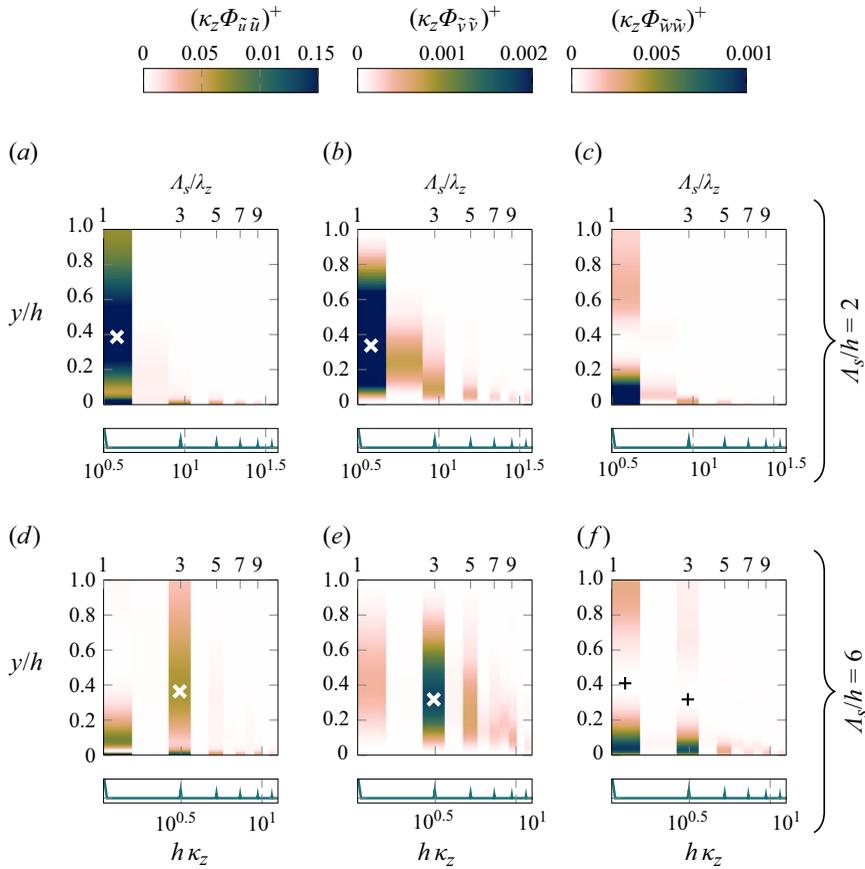
Figure 6. Premultiplied one-dimensional energy spectra of the streamwise $(a,d;\ \kappa_z^+\Phi_{\tilde{u}\tilde{u}}^+)$, wall-normal $(b,e;\ \kappa_z^+\Phi_{\tilde{v}\tilde{v}}^+)$ and spanwise $(c,f;\ \kappa_z^+\Phi_{\tilde{w}\tilde{w}}^+)$ dispersive velocity components. All data at $Re_\tau = 500$. $(a,b,c)\ \Lambda_s/h = 2$; $(d,e,f)\ \Lambda_s/h = 6$. Below each panel, we show the spanwise power spectral density of the square-wave signal indicating whether the wall is rough (signal $= 1$) or smooth (signal $= 0$); such a power spectral density is zero almost everywhere. The harmonic number Λ_s/λ_z associated with each Fourier mode is shown at the top of each panel. Selected local extrema of each spectrum are marked as $\times$ (white, maxima) and $+$ (black, minima).

modes being taller in the wall-normal direction. This is seen for $\Lambda_s/h = 6$ (panel d): the amount of energy on the first harmonic at the centreline is unexpectedly negligible, whereas most of the energy is found on the third harmonic. Similarly, the third harmonic of the $\tilde{v}$ distribution (panel e) has the largest energy values throughout the channel height. This behaviour can also be observed without premultiplication of the spectrum; it is not as pronounced at the lower Reynolds number ($Re_\tau = 180$).

Although the roughness pattern significantly excites the first harmonic, it fails to leverage a secondary motion of matching size if its period is too large ($\Lambda_s/h = 6$); rather, the response of the flow contains a substantial amount of energy on a narrower – but still h-scaled – wavelength. The wavelength of the dominant harmonic ($\lambda_z = 2h$) of panels (d,e) suggests this might be linked to the observed confinement of secondary motions to a $2h$-wide region about the spanwise surface transitions (see figure 4e). As confirmed by a separate analysis of artificial signals, this is likely true for the pattern of $\tilde{v}$. The $\tilde{u}$-spectrum must be interpreted with care instead: the dominance of the $\lambda_z = 2h$ mode might be an artefact caused by the specific value ($\Lambda_s = 6h$) of the period of the roughness

pattern. Roughness transitions are flanked by a high- and a low-momentum pathway, each of which has a $1h$ width. The remaining space between adjacent roughness transitions is then occupied by a local-equilibrium region where $\tilde{u}$ has opposite sign with respect to the secondary-motion-induced momentum pathways that surround it. This equilibrium region has a width of $3h - 2h = 1h$, so that effectively the spanwise $\tilde{u}$ distribution at the centreline is well described by a sinusoid of period $2h$. This is captured by the Fourier transform, whose dominant mode is not the first harmonic, but rather that with a $2h$ wavelength. If the strip width were larger, the width of the anti-correlation region would likely remain constant, whereas the equilibrium region would get larger. In this case, the first harmonic might be dominant even at the centreline (depending on the relative intensity between the values of $\tilde{u}$ in the equilibrium and anti-correlation regions).

Several wall-normal gaps, or minima, can be observed in the vertical stripes of the spectra. Most w-modes contain one such gap: as an example, in figure 6(*f*), at $y/h = 0.4103$ (first harmonic, see the mark in figure) and $y/h = 0.3181$ (third harmonic). Analogous minima of the spectrum can be observed for the remaining energy-containing modes (as well as in panel *c*) by adjusting the colour scale. We interpret these minima to be the centres of rotation of the circulatory motions associated with each of these Fourier modes. Indeed, w-energy is expected at the bottom and top of these wall-attached circulatory motions as previously shown. Also, coherently with our previous observations, $\tilde{v}$ energy is not seen at the wall; rather, its global maximum is seen between $y/h \approx 0.3$ and $y/h \approx 0.4$ ($y^+ \approx 150-200$) both for $\Lambda_s/h = 2$ and $\Lambda_s/h = 6$ (first harmonic in panel *b* and third one in panel *e*, respectively; see the marks in the figure). A local maximum of $\tilde{u}$-energy is seen on matching harmonics at matching wall-normal positions, consistently with the idea that the $\tilde{u}$ pattern is generated by $\tilde{v}$ transporting the mean velocity profile U. Finally, we suggest that the short energy gap seen at the wall on the first $\tilde{u}$-harmonic for the $\Lambda_s/h = 6$ case is linked to the change in sign seen in physical space at a matching wall-normal distance at the centre of each strip.

5. Decaying secondary motions

We now turn our attention to the time evolution of the secondary motions. As explained in § 2, their decay is triggered by suddenly removing the roughness strips from the walls. The process happens at a constant pressure gradient; the sudden removal of the roughness allows the flow rate to increase, as shown in figure 7(*a*) for two combinations of Λ_s and Re_τ chosen as an example. Coherently with (2.4), the increase in bulk velocity is driven by a temporary drop of the wall shear stress. As the flow approaches a new steady state for $t \to \infty$, the inner-scaled wall shear stress recovers its typical unitary value; however, this final equilibrium is reached at a point in time that exceeds the duration of our simulations, which only capture the decay of the dispersive velocity field. In other words, the spanwise-averaged field U evolves at a different rate from that of secondary motions.

Videos of the decaying dispersive velocity field are available (see *Supplementary data* at the end of § 7); as an example, snapshots at two different instants of time are shown in figure 7 for $Re_\tau = 500$, (*b,c*) $\Lambda_s/h = 2$ and (*d,e*) $\Lambda_s/h = 6$. The typical qualitative picture of the decay for low values of Λ_s/h, which is well represented by panels (*b,c*), is rather straightforward. The secondary motions slowly fade away, while the intense $\tilde{u}$ pattern at the wall quickly diffuses. A different behaviour is seen for higher strip widths ($\Lambda_s/h = 6$, panels *d,e*) at both the investigated Reynolds numbers: at $t = 0$ (steady state), the equilibrium region at the centre of each strip shows opposite values of $\tilde{u}$ with respect

(a)

(b)

(c)

(d)

(e)
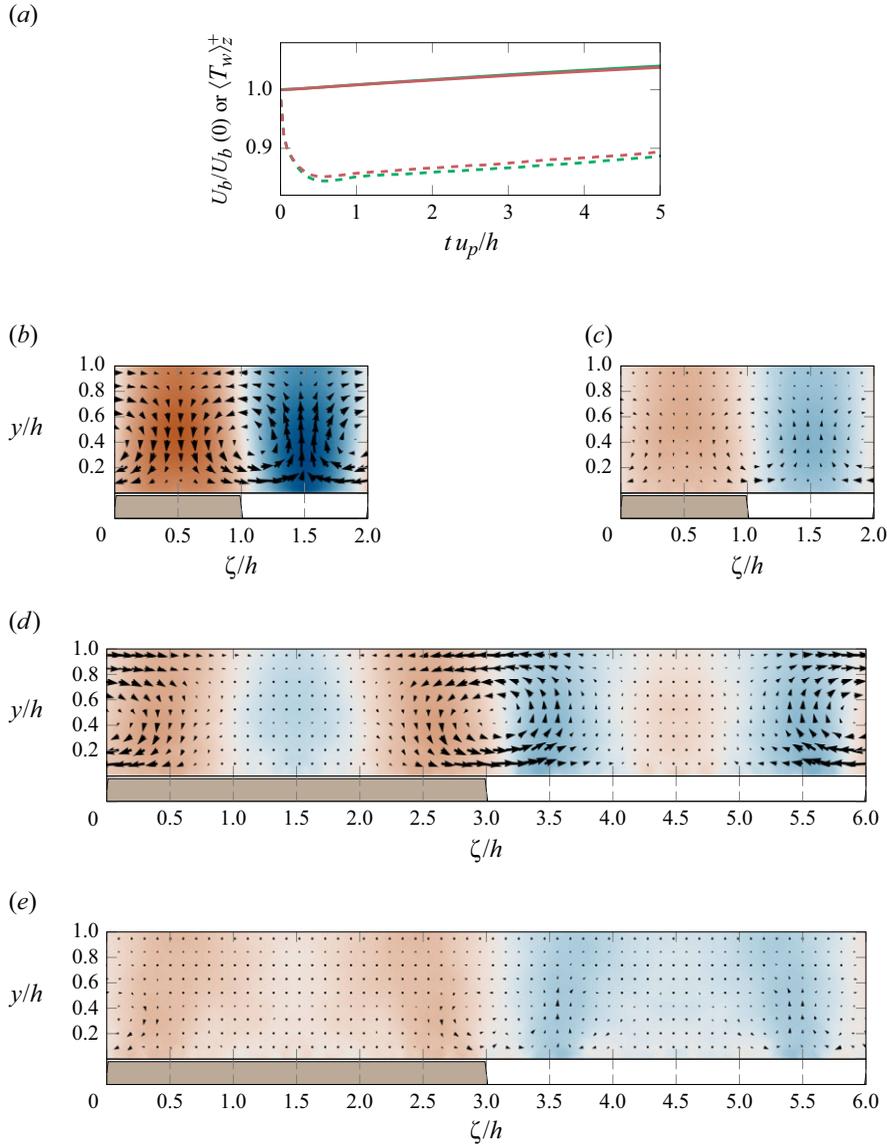
Figure 7. Time evolution (*a*) of the bulk velocity (solid, $U_b/U_b(0)$) normalised by its initial, steady-state value and of the inner-scaled spanwise-averaged wall shear stress (dashed, $\langle \tau_w \rangle_z^+$); $Re_\tau = 500$, $\Lambda_s/h = 2$ (green, as of table 1) and $\Lambda_s/h = 6$ (red). Decaying dispersive velocity field: $Re_\tau = 500$, $\Lambda_s/h = 2$, (*b*) $t = 1h/u_p$ and (*c*) $t = 3.2h/u_p$. Panels (*d,e*): same as panels (*b,c*), but for $\Lambda_s/h = 6$. Colour and arrow lengths as in figure 4. Below each panel, a grey fill indicates portions of the wall that were rough at the initial condition.

to the flanking regions where the secondary motions appear (see figure 4*e*). This still holds true at $tu_p/h = 1$ (figure 7*d*), although the regions of $\tilde{u}$ that are anti-correlated to $\tilde{v}$ lose their triangular shape (as evident in figure 4*e* at $t = 0$) and become rather invariant in the wall-normal direction. Advancing in time, the equilibrium region is progressively filled with momentum of the opposite sign; eventually ($tu_p/h = 3.2$, figure 7*e*), the sign of the dispersive velocity is roughly uniform across each strip. It is unlikely that this switch of the sign of $\tilde{u}$ in time is caused by $\tilde{v}$-transport of the U field, as $\tilde{v}$ is not particularly intense in this region.

5.1. *Volume-averaged dispersive energy*

As discussed in section § 3.4, the time needed for the dispersive field (or, to be more precise, by some of its features) to decay can be quantified by defining some energy measure and by tracking it in time. When the rough strips are removed from the walls of the channel, the dispersive velocity field starts losing energy with respect to the steady-state condition over strip-type roughness. A time scale for the decay can be then defined as the time needed by a generic energy measure to lose 85 % of its initial value. In particular, the volume-averaged energy of the momentum pathways (I_u, see (3.20)) and of the circulatory motions (I_{vw}, see. (3.21)) will be used in this section to calculate two corresponding time scales (T_u and T_{vw}, see § 3.4 and (3.19)). Using volume-averaged quantities yields easy-to-interpret results at the cost of neglecting the spatial complexity of the flow; an attempt to recover some of this spatial complexity will be later done in § 5.2 and in Appendix B.

The initial steady-state values of I_u and I_{vw} are shown in figure 8(*a–d*) for each available flow configuration; panels (*e–h*) show their time evolution. At the lower Reynolds number (figure 8*a,b*), motions with $1 \leqslant \Lambda_s/h \leqslant 4$ hold a similar amount of energy independently of their size. This contradicts the observation (Wangsawijaya & Hutchins 2022) that structures of period $\Lambda_s \approx 2h$ ($s \approx h$) are more energetic than those of any other size; we suggest this discrepancy to be a consequence of the low Reynolds number. Indeed, low-Re data suffers from two issues. It is known, for instance, that linear transient growth analysis predicts large structures to show significant values of transient growth only for sufficiently high Reynolds numbers (Cossu *et al.* 2009); moreover, large-scaled outer-layer eddies only become significantly energetic in channel flows if the Reynolds number is high enough (Lee & Moser 2015). It can be thus expected that if the flow acts to favour structures of a specific outer-scaled size, this would only be seen at a sufficiently high Reynolds number. Our data at $Re_\tau = 500$ (panels *c,d*) confirm this line of reasoning: the energy held by secondary motions is maximum for $\Lambda_s = 2h$ as expected. A second issue with low-Re data is given by the lack of scale separation: at the considered Reynolds number ($Re_\tau = 180$), the outer-layer length scale h is equivalent to $180 \, \delta_v$. Such a value is not too far from the dominant spanwise scale of near-wall structures ($100 \, \delta_v$, see Kline *et al.* 1967). In other words, we cannot easily tell whether the secondary motions that we impose are inner- or outer-scaled. Care must be then exerted in interpreting low-Re data.

As for the time evolution of the volume averages (figure 8*e–h*), they typically show a monotonically decreasing trend both for the streamwise and circulatory patterns. There are, however, notable exceptions. At low Reynolds number (panel *e*), the energy of the streamwise pattern temporarily exceeds its initial value for $\Lambda_s/h = 4$, to then decay as expected; similarly, it temporarily increases after an initial decay for $\Lambda_s/h = 6$. Most importantly, at the higher Reynolds number (panel *g*) the volume-averaged energy monotonically decays in all cases, except for the energy of the streamwise pattern for $\Lambda_s/h = 2$ and $\Lambda_s/h = 4$. An excess of streamwise energy with respect to the initial condition is seen for these cases. To better illustrate our findings, we define a transient growth coefficient G_u:

$$G_u = max_t \frac{I_u(t)}{I_u(0)} \tag{5.1}$$

and plot it against the size of the secondary motions in figure 9(*a,b*). At $Re_\tau = 180$ (panel *a*), transient growth is only observed for $\Lambda_s/h = 4$ and is not particularly pronounced (3 %). At $Re_\tau = 500$ (Panel *b*), a modest (6 %) transient growth of the dispersive $\tilde{u}$-energy is seen for $\Lambda_s/h = 2$; a larger growth (13 %) is seen for $\Lambda_s/h = 4$. The confidence level on the occurrence of transient growth given the statistical uncertainty
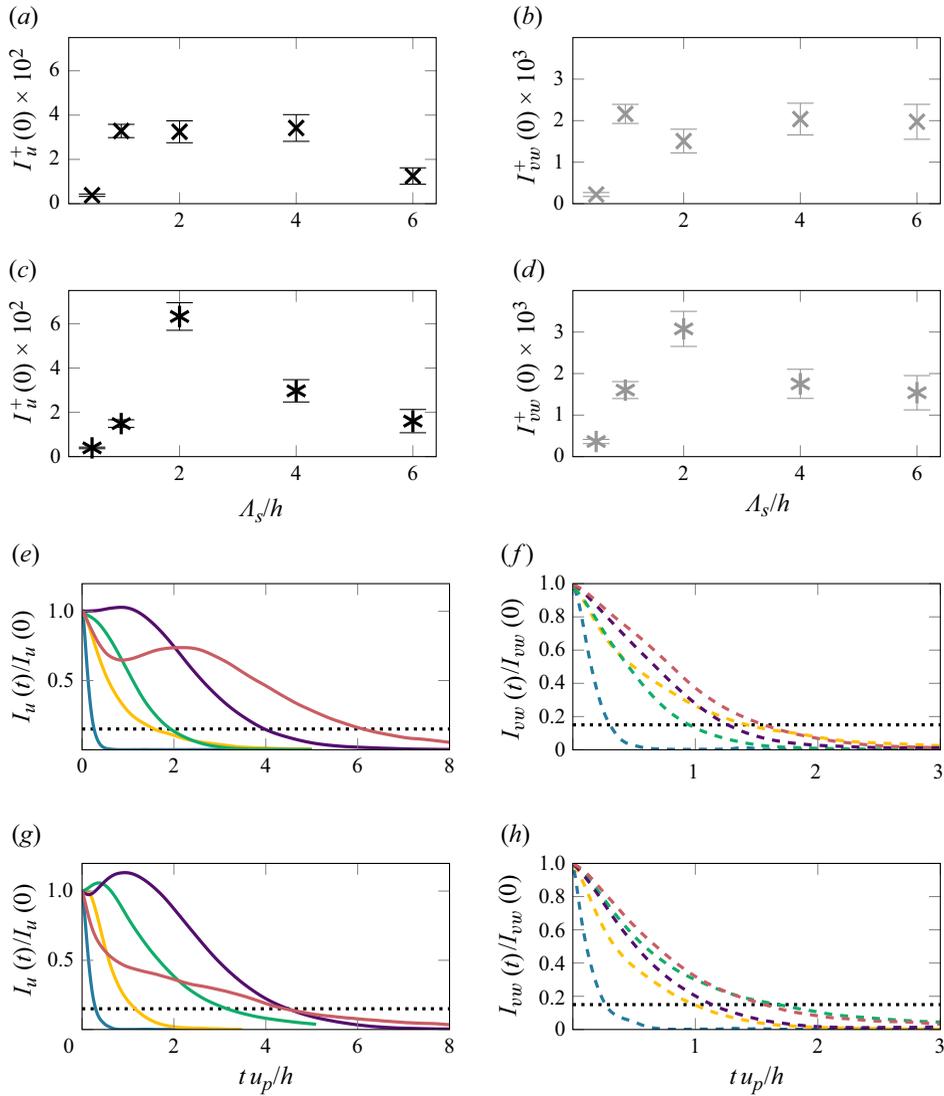
Figure 8. Volume-averaged dispersive energy. Initial (steady-state) values of the volume-averaged energy for varying spanwise period Λ_s of the roughness pattern: (a) I_u^+, $Re_\tau = 180$; (b) I_{vw}^+, $Re_\tau = 180$; (c,d) same as panels (a,b), but at $Re_\tau = 500$. The error bars indicate the 95 % confidence interval, estimated as per § 3.5. Time evolution of the volume-averaged energy normalised by its initial value: (e) $I_u(t)/I_u(0)$, $Re_\tau = 180$; (f) $I_{vw}(t)/I_{vw}(0)$, $Re_\tau = 180$; (g–h) same as panels (e–f), but at $Re_\tau = 500$. The horizontal dotted line indicates the threshold value used for the calculation of the time scale (see (3.19)). Colour legend as in table 1: ■ $\Lambda_s/h = 0.5$; ■ $\Lambda_s/h = 1$; ■ $\Lambda_s/h = 2$; ■ $\Lambda_s/h = 4$; ■ $\Lambda_s/h = 6$.

is estimated in Appendix A to be 78.9 % and 85.2 % for $\Lambda_s/h = 2$ and $\Lambda_s/h = 4$, respectively, at $Re_\tau = 500$. No excess energy is seen for other values of Λ_s at the higher Reynolds number, except for a negligible transient growth for $\Lambda_s/h = 1$. It appears that, for $2 \leqslant \Lambda_s \leqslant 4$, the generation of the high- and low-momentum pathways continues for a short time even after removing the rough strips that enable their sustainment. This might be evidence in favour of the hypothesis of Townsend (1976), who predicted that structures of this size ($\Lambda_s \leqslant 4$) would be able to self-sustain: not only do the momentum pathways maintain their energy for a short time, but they even show excess energy with respect to the
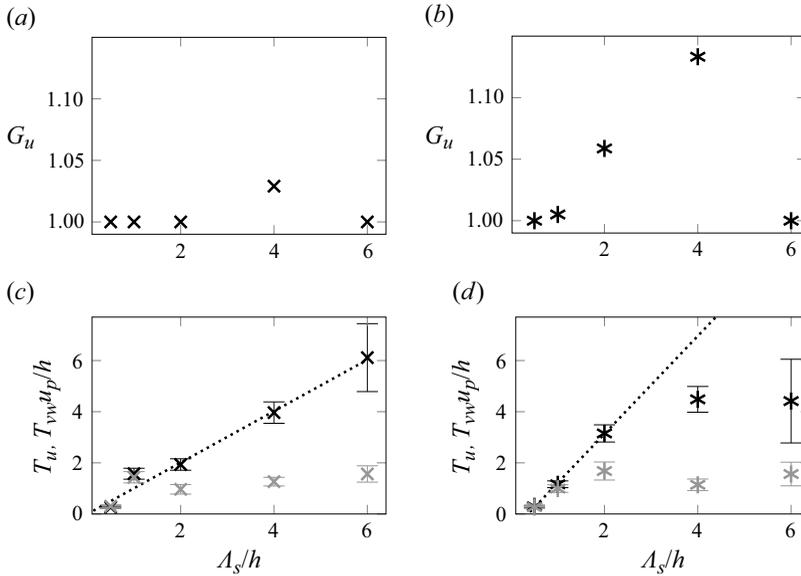
Figure 9. Transient growth G_u of the streamwise volume-averaged dispersive energy $I_u(t)$; (*a*) $Re_\tau = 180$, (*b*) $Re_\tau = 500$. The confidence level on the occurrence of transient growth is estimated in Appendix A. Time to decay (as defined per (3.19) applied to I_u and I_{uv}) for the streamwise (T_u, black) and circulatory (T_{vw}, grey) dispersive energy; (*c*) $Re_\tau = 180$, (*d*) $Re_\tau = 500$. The dotted line represents a linear fit for T_u performed (*c*) by rejecting data at $\Lambda_s/h = 1$ and (*d*) by only considering data for $\Lambda_s/h \leqslant 2$. Error bars indicate the 95 % confidence interval estimated as per § 3.5.

initial conditions. The excess energy is also reminiscent of linear transient growth analysis and its results (Del Álamo & Jiménez 2006), in the sense that we observe transient growth of I_u before its decay. Moreover, the spanwise periods at which we observe transient growth ($\Lambda_s/h \approx 2-4$) are in good agreement with the spanwise wavelength of maximum linear transient growth ($\lambda_z/h = 3$) found by the aforementioned study. There is, however, a crucial difference between our simulations and linear transient growth analysis, apart from the obvious nonlinearity of our system. Linear transient growth analysis studies the evolution of a perturbation of a given size, whereas we study the evolution of a fully developed structure.

In linear transient growth analysis, the transient growth of *u*-energy is found to be driven by the v component through transport of the mean field (Del Álamo & Jiménez 2006). Similarly, in §§ 3.3 and 4, we have proposed the formation of the $\tilde{u}$ momentum pathways might be driven by $\tilde{v}$ transport of the U-field (dispersive production). It could be expected, then, that this same mechanism would drive the initial overshoot of I_u energy that we observe. If this were the case, we would expect I_{vw} to be able to maintain its initial energy for a longer time in cases for which excess I_u is seen, or perhaps to decay slower than in other cases. A preliminary scrutiny of figure 8(*f,h*) suggests this is not the case: no initial plateau of I_{vw} is seen for values of Λ_s at which transient growth is observed. Moreover, we could not find any link between the rate of change of I_{vw} at $t = 0$ and the occurrence of transient growth. We further investigate the matter by calculating a time scale for the decay of I_u and I_{vw} based on the definition in (3.19). The resulting time scales are T_u and T_{vw}, respectively. Results are shown in figure 9(*c,d*) and are scaled with h/u_p, as this time scale remains constant in physical terms across different simulations at the same Re_τ. Notice that one data point (the value of T_u at $Re_\tau = 500$, $\Lambda_s/h = 6$, panel *d*) is affected by a significant amount of statistical uncertainty; the reasons for this

can be multiple. On the one hand, this flow case might exhibit unexpectedly large velocity fluctuations, leading to a large statistical uncertainty on the dispersive velocity field (the uncertainty then propagates to I_u and T_u). On the other hand, the dispersive velocity field is computed by performing, among others, a phase average over multiple spanwise periods (see § 2). For such a value of $\Lambda_s/h = 6$, the simulation box ($L_z/h = 6$) only contains one period Λ_s, so that no phase average is effectively performed. This might explain the increased statistical uncertainty of the flow case under consideration; in all other flow cases at the same Reynolds number, the simulation box contains at least two spanwise periods Λ_s (see table 1) which can be exploited by the phase average. Finally, notice that the low-Re simulation with matching Λ_s (namely, $Re_\tau = 180$, $\Lambda_s/h = 6$, panel *a*) also has a relatively large statistical uncertainty; in this last case, nevertheless, it was possible to produce a larger number of repetitions of the simulation (as low-Re simulations are cheap) so as to mitigate the statistical variability.

At the lower Reynolds number, T_{vw} generally increases with Λ_s, though the circulatory motions remain in the flow for an unexpectedly long time for $\Lambda_s/h = 1$. At the higher Reynolds number, T_{vw} increases with Λ_s until it reaches a local maximum value for $\Lambda_s/h = 2$. For larger values of Λ_s, the circulatory motions remain confined in a $2h$-wide region around roughness transitions (see figure 4), so that effectively they stop growing in size. Similarly, their time to decay remains bounded to $T_{vw} \leqslant 2$ (roughly). The local maximum of T_{vw} for $\Lambda_s/h = 2$ might suggest that the longer-living circulatory motion is able to leverage production of I_u for a longer time, causing the observed overshoot of I_u. However, data at $\Lambda_s/h = 4$ contradict this idea: for this value of Λ_s, I_u undergoes an even stronger transient growth – and yet the circulatory motion decays in an unexpectedly short time. More generally, momentum pathways tend to live longer than the circulatory motions (as $T_u > T_{vw}$ in most cases). In §§ 3.3 and 4, we have argued that the momentum pathways are mostly produced by the circulatory motions through the dispersive production term: the observed delay in the decay of I_u with respect to I_{vw} supports this idea. Indeed, the streamwise dispersive field $\tilde{u}$ has its own dynamics, as indicated by (3.17); it is reasonable that it would be able to survive for a limited time after the circulatory motions have decayed. The absence of circulatory motions simply means that the $\tilde{u}$ field is not being fed energy by the dispersive production term anymore; the viscous dissipation will then gradually erode the remaining $\tilde{u}$-energy until the decay is complete. In spite of the relevance of the dispersive production term, the variability of T_{vw} fails to predict the variability of T_u, indicating that production through $\tilde{v}$-transport of U alone cannot explain the dynamics of I_u. Indeed, as once again highlighted in (3.17), the dynamics of $\tilde{u}$ is affected by several other terms.

The time to decay of I_u generally linearly increases with the spanwise periodicity Λ_s at the lower Reynolds number; at the higher Re, it also generally increases, although the slope of the trend diminishes for $\Lambda_s/h > 2$. There might be an exception to this monotonically increasing trend: the estimated value of T_u for $\Lambda_s/h = 6$, $Re_\tau = 500$ (figure 9*d*) is essentially equal to that seen for $\Lambda_s/h = 4$ at the same Reynolds number. However, data at $\Lambda_s/h = 6$ are affected by a significant statistical uncertainty, making it impossible to assess whether the trend of T_u effectively saturates, starts decreasing or keeps increasing (albeit with a smaller slope) for high Λ_s. Interestingly, the observed transient growth of I_u has no strong influence on T_u: at $Re_\tau = 500$ (panel *d*), the value of T_u for $\Lambda_s/h = 2$ is either lower or comparable (accounting for the statistical uncertainty) than that for $\Lambda_s/h = 6$. Notice that transient growth is observed for $\Lambda_s/h = 2$, but not for $\Lambda_s/h = 6$. An additional noteworthy feature can be found in the low-Re data of panel (*c*): momentum pathways of period $\Lambda_s = h$ subsist in the flow longer than what could be expected by extrapolating the observed trend. Although this could be a sign of the flow favouring these

specific h-scaled structures, it should be kept in mind that the structures might as well be inner-scaled owing to the lack of scale separation. As previously explained, a $1h$ period is indeed equivalent to $180\delta_v$ in wall units at $Re_\tau = 180$; such an inner-scaled value of the period is not far from the typical spanwise spacing of buffer-layer small scales ($100\delta_v$, see Kline *et al.* 1967).

Starting from the temporal information we gather, we now estimate the streamwise distance needed for the $\tilde{u}$ pattern (that is, for the high- and low-momentum pathways) to decay. This enables the comparison of our results with other studies measuring the streamwise coherence of momentum pathways (e.g. Womack *et al.* 2022). First, we find a linear fit to the trend of T_u against Λ_s; at $Re_\tau = 180$, we exclude the datapoint at $\Lambda_s/h = 1$, whereas at $Re_\tau = 500$, only the values $\Lambda_s/h \leqslant 2$ are considered. Although this is a rough approximation, the fit (shown by a dotted line in figure 9c,d) correctly captures the order of magnitude of T_u over the considered values of Λ_s. Then, we estimate the streamwise distance Δx_d needed for the decay of momentum pathways as $\Delta x_d = U_{b,s} T_u$, where $U_{b,s}$ is the bulk velocity seen at a matching value of Re_τ between smooth walls. The underlying idea is that structures are advected downstream as they evolve and that the bulk velocity is the mean velocity at which this happens. Using the value of the bulk velocity seen between smooth walls is an arbitrary choice; again, it is only meant to roughly capture the order of magnitude of Δx_d. The following crude estimates are obtained:

$$\Delta x_d \approx 15.8 \, \Lambda_s \qquad \text{at } Re_\tau = 180,$$
$$\Delta x_d \approx 34.9 \, \Lambda_s - 12.7h \qquad \text{at } Re_\tau = 500 \text{ for } \Lambda_s/h \leqslant 2. \tag{5.2}$$

The order of magnitude of our estimates for a spanwise wavelength $\Lambda_s = h$ is $\Delta x_d \approx 15 - 20$; this is in line with the experiments of Womack *et al.* (2022), who reported the streamwise extent of momentum pathways to be $18h$ at least.

As already discussed, the value of the time scale T_{vw} associated with the circulatory motions saturates for high values of Λ_s. One way of explaining the observed saturation could be given by the findings of Lozano-Durán & Jiménez (2014). The authors identified and tracked naturally occurring structures that are both wall-attached and associated with $u'v'$-anticorrelation events; they found the lifetime T_{ae} of these structures to be proportional to their half-height h_y,

$$T_{ae}^+ \approx 2h_y^+. \tag{5.3}$$

In the case of the present study, the time scale T_u cannot be considered to be analogous to T_{ae}, as it measures the lifespan of a velocity pattern that is not necessarily wall-attached and that includes regions in which $\tilde{u}$ and $\tilde{v}$ are positively correlated. The circulatory motions, instead, satisfy these two requirements: they extend upwards from the near-wall region and they are responsible for the $\tilde{u}$-$\tilde{v}$ anticorrelation (see § 4). Thus, although the secondary motions are not features of the fluctuation field (differently from the structures observed by Lozano-Durán & Jiménez 2014), we will try to draw an analogy between T_{vw} and T_{ae}. By making (5.3) dimensional, we expect:

$$T_{vw} \approx 2\frac{h_y}{u_p} \quad \text{(expected)}. \tag{5.4}$$

To enable a comparison between our results and those of Lozano-Durán & Jiménez (2014), we now need to estimate the half-height h_y of the circulatory motions. We define a vortex centre as the point at which, simultaneously, $\tilde{v}$ changes in sign in z and $\tilde{w}$ changes in sign in y. The so-defined vortex centres are marked in figure 4 and satisfactorily represent the centre of the cross-sectional circulatory motions. The structure half-height h_y is then simply given by the wall-normal position of the vortex centre.
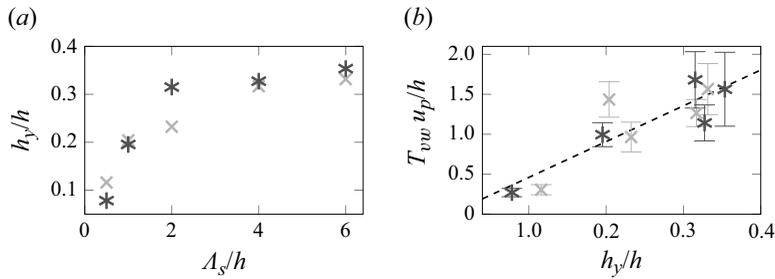
Figure 10. (*a*) Wall-normal position h_y of the vortex centre of the circulatory motions against the spanwise period Λ_s. (*b*) Time to decay T_{vw} of the circulatory motions against the wall-normal position h_y of the vortex centre. Light grey crosses indicate data at $Re_\tau = 180$; dark grey asterisks indicate data at $Re_\tau = 500$. In panel (*b*), a linear fit to all available data is shown as a dashed line; error bars indicate the 95 % confidence interval, estimated as per § 3.5.

Figure 10(*a*) shows how the half-height h_y changes with the spanwise period Λ_s of the roughness pattern. A good collapse of low- and high-Re data is observed. The circulatory motions get taller for increasing Λ_s; as Λ_s approaches large values (say, $\Lambda_s / h \geqslant 2$), the growth of h_y slows down. This saturation effect is expected: as can be seen from figure 4, the circulatory motions fill the entire channel half-height for $\Lambda_s / h \approx 2$, so that their wall-normal growth is phyisically limited for larger values of Λ_s. As the structures stop getting taller, they also become confined to a region surrounding roughness transitions (see § 4): it appears that the circulatory motions roughly maintain their y-z aspect ratio – in a way that is reminiscent of the attached eddy hypothesis (Marusic & Monty 2019). Finally, we compare our data to those of Lozano-Durán & Jiménez (2014) by plotting the time scale T_{vw} of the circulatory motions against their half-height h_y in figure 10(*b*): owing to (5.4), a linear trend is expected. Although the data do not appear to collapse on a single line, their dispersion appears to be directional, so that a linear fit is reasonable. By considering both low- and high-Re data, we obtain

$$\frac{T_{vw,fit}}{h/u_p} = 4.48 \frac{h_y}{h} + 0.011. \tag{5.5}$$

Although the intercept of our fit is small (and thus in agreement with (5.3)), the slope we obtain is roughly two times larger than expected. This quantitative difference can be explained by the fact that we track different structures with respect to Lozano-Durán & Jiménez (2014); moreover, we use different definitions of the time scale and of the structure half-height – all of which are arbitrary. To conclude, the ansatz of (5.3) does not fully explain the variability of T_{vw}, but it correctly captures the general trend of larger values of h_y being typically associated with larger values of T_{vw}. Then, the fact that the circulatory motions stop growing in size for large values of Λ_s can help explain the observed saturation of T_{vw}.

5.2. *Plane-averaged dispersive energy: the decay of the wall shear stress pattern*

Albeit easily interpretable, volume-averaged quantities hide the spatial complexity of the observed phenomena. To recover information in the wall-normal direction, we inspect the average i_u (defined in (3.22)) of the streamwise dispersive energy on wall-parallel planes. Bear in mind that, as discussed in § 3.2, the value of i_u seen at a given wall-normal position is equal to the sum of the contributions of each Fourier mode of the spectrum $\Phi_{\tilde{u}\tilde{u}}$ at the same distance from the wall.
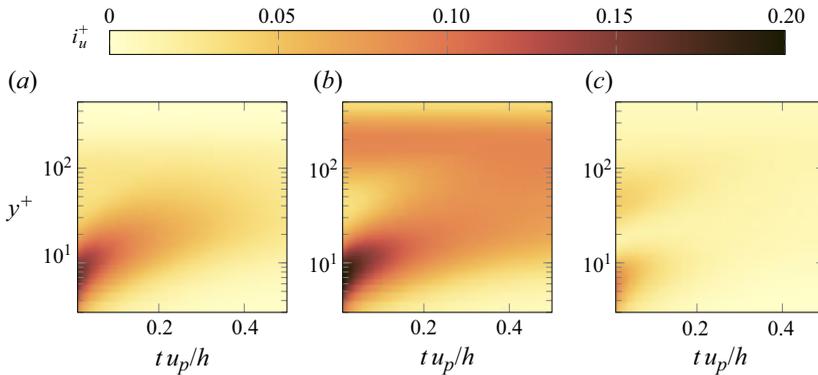
Figure 11. Time evolution of the plane-averaged dispersive energy i_u^+ of the streamwise dispersive velocity. Please notice that, in spite of the logarithmic scale on the vertical axis, no premultiplication is used; consequently, the visual representation given by this figure is not well representative of the total (integral) amount of energy contained in different regions of the channel. All data at $Re_\tau = 500$; (a) $\Lambda_s/h = 1$, (b) $\Lambda_s/h = 2$ and (c) $\Lambda_s/h = 6$.

The plane-averaged energy i_u is shown in figure 11 for a selection of flow cases at $Re_\tau = 500$ for a short time interval after the spanwise heterogeneity has been removed. Notice that no premultiplication is performed for this figure despite the log-scaled vertical axis: this is done to better highlight its near-wall features. As a consequence, though, the total amount of energy contained in the outer layer is misrepresented by the visualisation of figure 11. Similarly to what has been observed in figures 4 and 6, two separate energy peaks can be identified in figure 11 at the initial condition ($t = 0$, steady state) for large enough values of Λ_s/h: one in the viscous sublayer ($y^+ \leqslant 10$), one further away from the wall. This second peak is particularly pronounced for $\Lambda_s/h = 2$ ($y^+ \approx 200$, panel b), and not particularly so for $\Lambda_s/h = 6$ ($y^+ \approx 50$, panel c); it is not observed at the lower Reynolds number or, at least, it is not as pronounced. In general, the streamwise pattern for $\Lambda_s/h = 6$ is much less energetic than that for $\Lambda_s/h = 2$, as previously observed by analysing volume averages (figure 8c). The common feature of all data in figure 11 (which is also observed for values of Λ_s and Re_τ that are not shown) is that the near-wall peak diffuses towards the core of the channel. Our steady-state analysis of the streamwise momentum budget (§ 4) suggests that viscous diffusion is responsible for this process. The near-wall peak is associated with the near-wall square-wave distribution of $\tilde{u}$ seen in figure 4, and hence to the spanwise distribution of wall shear stress.

While the near-wall pattern of $\tilde{u}$ is particularly intense, it resides in a restricted region of the channel that shrinks in size as Re_τ increases. As a consequence, its contribution to the volume-averaged energy is marginal, so that the time scales measured in figure 9 are not representative of the decay of the dispersive wall shear stress distribution. A suitable time scale for this purpose could be defined, for instance, by applying the definition in (3.19) to the plane-averaged energy i_u at the wall. Instead, we go one step further and analyse the individual contributions to i_u of each Fourier mode (as per (3.8)) and measure their time to decay. In other words, we apply the definition in (3.19) of the time scale to the spectrum $\Phi_{\tilde{u}\tilde{u}}$ – evaluated at the first wall-normal grid point ($y^+ \approx 1$, please refer to table 1) to be representative of the wall shear stress. In this way, we obtain a different time scale $T_w(\lambda_z)$ for each Fourier mode (of wavelength $\lambda_z = 2\pi/\kappa_z$) that constitues the pattern of wall shear stress.
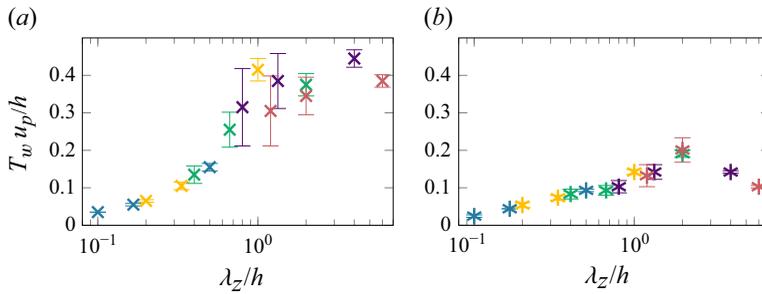
Figure 12. Time to decay $T_w(\lambda_z)$ of the Fourier harmonics (represented by their wavelength λ_z) that compose the dispersive wall shear stress distribution, calculated by applying the definition in (3.19) to the spectrum $\Phi_{\tilde{u}\tilde{u}}$ (shown in figure 6) at $y^+ \approx 1$. Only the first three odd energy-containing harmonics are shown. (*a*) $Re_\tau = 180$; (*b*) $Re_\tau = 500$. The error bars indicate the 95 % confidence interval, estimated as per § 3.5. Colour legend as in table 1: ■ $\Lambda_s/h = 0.5$; ■ $\Lambda_s/h = 1$; ■ $\Lambda_s/h = 2$; ■ $\Lambda_s/h = 4$; ■ $\Lambda_s/h = 6$.

Results are shown in figure 12, which collates data for all available values of Λ_s/h. Only the first three energy-containing harmonics are shown; higher harmonics hold little energy so that the signal-to-noise ratio is excessively low. Patterns of wall shear stress of different period Λ_s may contain Fourier modes with the same (or similar) spanwise wavelength λ_z. The time needed for Fourier modes of comparable wavelengths from different simulations (different Λ_s/h) to decay is similar: data from different simulations at the same Re_τ appear to collapse on the same curve. In other words, it appears that the time evolution of the Fourier modes is influenced by their own wavelength λ_z (and, of course, by the Reynolds number), but not much by the geometry of the problem (that is, by Λ_s/h) or by the amount of energy they hold at the initial steady state. As an example, the first harmonic of figure 6(*a*) and the third one in figure 6(*d*) hold a different amount of energy at the wall at the initial steady state; yet, they share the same spanwise wavelength $\lambda_z/h = 2$ and take a comparable amount of time to decay as measured by T_w (see figure 12).

Figure 12(*a*) shows data at $Re_\tau = 180$: the time to decay increases with the wavelength until $\lambda_z/h = 1$ to then saturate for larger values of λ_z/h. At the higher Reynolds number (figure 12*b*), instead, the time to decay increases up until its peak value at $\lambda_z/h = 2$ to then decrease for higher values of the wavelength. That is, Fourier modes of the wall shear stress with $\lambda_z/h = 2$ are the longest-lived ones. This value of the wavelength matches the period $\Lambda_s/h = 2$ for which secondary motions are the most energetic.

We interpret the above observations as follows. The longer time to decay might be a sign that near-wall Fourier modes of a specific wavelength ($\lambda_z/h = 2$ at $Re_\tau = 500$) are less damped (e.g. by viscous dissipation) than the remaining modes during their evolution. This does not help to explain the generally increasing trend of T_u against Λ_s seen in figure 9(*d*): T_u measures indeed the time to decay of a quantity that is integrated in the wall-normal direction over the entire channel half-height. Nevertheless, the near-wall behaviour discussed here might play a crucial role in the formation of secondary motions. Consider, for instance, a fully developed flow suddenly hitting a patch of spanwise heterogeneous roughness. The roughness can be idealised as a disturbance applied to the near-wall region; in light of the above discussion, we would expect disturbances of a specific size to be less damped than others in this region, so that they grow more energetic. This mechanism might help to explain why secondary motions with a spanwise period of $\Lambda_s/h = 2$ are the most energetic at $Re_\tau = 500$ (see figure 8*c*); bear in mind that a spanwise roughness pattern of period Λ_s significantly excites the Fourier mode with wavelength $\lambda_z = \Lambda_s$ (as can be seen from the spectra of the roughness patterns in figure 6).
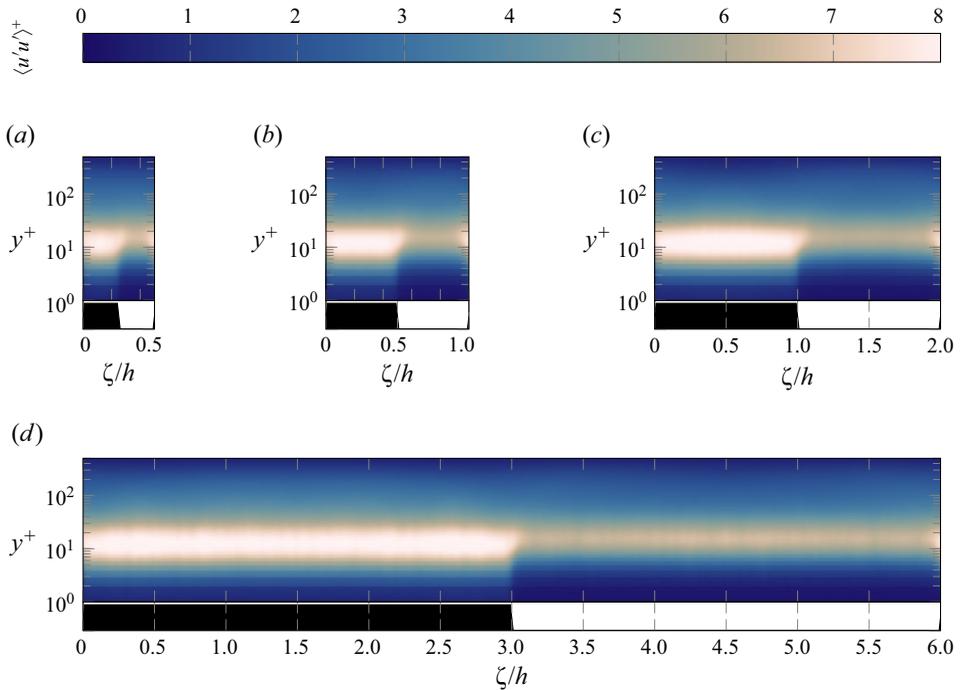
Figure 13. Distribution of the Reynolds stress $\langle u'u' \rangle$ over strip-type roughness at a steady state. The bar below each panel indicates regions of rough (black) or smooth (white) wall. Please notice that, in spite of the logarithmic scale on the vertical axis, no premultiplication is used. (*a*) $\Lambda_s/h = 0.5$; (*b*) $\Lambda_s/h = 1$; (*c*) $\Lambda_s/h = 2$; (*d*) $\Lambda_s/h = 6$. All data at $Re_\tau = 500$.

6. The fluctuation field

So far, we have inspected the time evolution of the dispersive velocity field, as it is contains the information regarding the high- and low-momentum pathways which are of interest for this study. Nevertheless, the fluctuation field also contains valuable information: the secondary flows investigated here are commonly understood to be of Prandtl's second kind (Wang & Cheng 2006; Anderson *et al.* 2015; Hwang & Lee 2018), meaning that they are driven by turbulence and arise owing to lateral dishomogeneities of the Reynolds stresses. For completeness then, and as an example, we analyse the normal Reynolds stress $\langle u'u' \rangle$ to recover some information about the fluctuation field, as this stress is usually the dominant term of the turbulent kinetic energy. Figure 13 shows its distribution at the initial steady state in the presence of strip-type roughnes for a selection of flow cases at $Re_\tau = 500$. Fluctuation intensites are roughly uniform over each smooth or rough strip; strong lateral changes of $\langle u'u' \rangle$ are only seen at roughness transitions. Typically, $\langle u'u' \rangle$ is maximum in the buffer layer ($y^+ \approx 10$); as would be expected from the viscous scaling of near-wall turbulence, this maximum is more energetic and closer to the wall over rough strips than over smooth ones for all tested values of Λ_s. Interestingly, then, the energy of u' fluctuations correlates well with the distribution of dispersive wall shear stress, although the fluctuations themselves are deprived of any coherent information owing to their definition. We interpret this as the random u'-fluctuations being modulated in amplitude (Mathis *et al.* 2009) by a coherent envelope, so that their amplitude (and thus, energy) is larger over rough strips. Notice that the position at which large spanwise gradients of the turbulent kinetic energy are found is indicative of the position of the circulatory motions.

1007 A19-32

We track the time evolution of this heterogeneity in the kinetic energy as follows. We average the value of $\langle u'u'\rangle$ in the buffer layer ($5 \leqslant y^+ \leqslant 30$) over rough or smooth strips alternatively; this defines the two quantities $\langle u'u'\rangle_R$ (averaged over portions of the wall that are, or were, rough) and $\langle u'u'\rangle_S$ (averaged over portions of the wall that are smooth from the initial condition). Similarly, we average the wall shear stress over rough or smooth strips to yield $\tau_{w,R}$ and $\tau_{w,S}$. Then, we define a quantitiy Δ_{uu} as the difference between the two averaged values of the kinetic energy, $\Delta_{uu} = \langle u'u'\rangle_R - \langle u'u'\rangle_S$. Positive values indicate that turbulence is more energetic over portions of the wall that were rough at the initial condition, whereas the opposite holds for negative values. A zero value of the difference indicates instead that the distribution of kinetic energy in the buffer layer has become homogeneous. Figure 14(*a,b*) shows, as an example, the evolution of $\langle u'u'\rangle_R$, $\langle u'u'\rangle_S$, $\tau_{w,R}$ and $\tau_{w,S}$ for a selected flow case ($Re_\tau = 500$, $\Lambda_s/h = 2$). As the rough strips are removed from the walls, the flow accelerates (as seen from figure 7a). This acceleration damps u'-fluctuations at all spanwise positions. Most of the loss in kinetic energy is seen for $\langle u'u'\rangle_R$; this loss is then quickly partially recovered before the system slowly approaches homogeneity. After an initial not so pronounced decrease, $\langle u'u'\rangle_S$ also increases to reach roughly the same value as $\langle u'u'\rangle_R$. Notice that less kinetic energy is found over a smooth strip at a steady state in the context of strip-type roughness than over a smooth homogeneous wall in a steady-state setting. As for the wall shear stress, a substantial decrease of $\tau_{w,R}$ is seen starting from the initial condition; $\tau_{w,R}$ then reaches a minimum – although such a minimum is not as pronouced as the minimum of $\langle u'u'\rangle_R$. Moreover, the minimum of $\langle u'u'\rangle_R$ is seen at an earlier time ($t = 0.196\,h/u_p$) than that of $\tau_{w,R}$ (at $t = 0.65\,h/u_p$), suggesting that fluctuations evolve at a faster pace than the wall shear stress. After the minimum, the wall shear stress $\tau_{w,R}$ roughly remains constant, whereas the value of $\tau_{w,S}$ slowly increases from its initial value to reach that of $\tau_{w,R}$.

The remaining panels of figure 14 show instead the initial value and the evolution of Δ_{uu} for all considered flow cases at the low (panels *c,d*) and high (panels *e,f*) Reynolds number. Notice that only a limited number of repetitions is available for $\Lambda_s/h = 0.5$, $Re_\tau = 180$; this is sufficient to achieve a satisfactory accuracy of first-order velocity momenta (e.g. the dispersive velocity), but not of the second-order ones needed in this case (e.g. $\langle u'u'\rangle$). Data for this specific combination of parameters are thus not shown. At the steady state, the difference in kinetic energy between rough and smooth strips increases with Λ_s at the lower Reynolds number, until it saturates for $\Lambda_s/h \geqslant 4$. At the higher Reynolds number, instead, it is maximum for $\Lambda_s/h = 4$. For all considered flow cases, the initial condition (consisting in higher energy over portions of the wall that are, or were, rough) is quickly reversed as the values of Δ_{uu} turn negative. For $\Lambda_s/h = 2$ and $\Lambda_s/h = 4$ at $Re_\tau = 500$, interestingly, the initial sign of Δ_{uu} is recovered at roughly $t = 0.3h/u_p$; advancing in time, sections of the wall that were rough maintain a slightly higher fluctuation intensity $\langle u'u'\rangle$ than the remaining ones for an extended period of time. These are the only two cases for which this behaviour is observed; interestingly, these are also the only two cases for which a significant overshoot of I_u is seen at the higher Reynolds number.

7. Summary and conclusion

We study the secondary motions found in turbulent channel flows in the presence of a spanwise-heterogeneous roughness pattern (strip-type roughness) of varying spanwise period Λ_s. The investigation is carried out both at a steady state and as the secondary motions decay towards a spanwise-homogeneous configuration. The decay is obtained by suddenly removing the strip-type roughness, so that the flow evolves between smooth walls. We are able to capture the temporal evolution of the secondary motions by
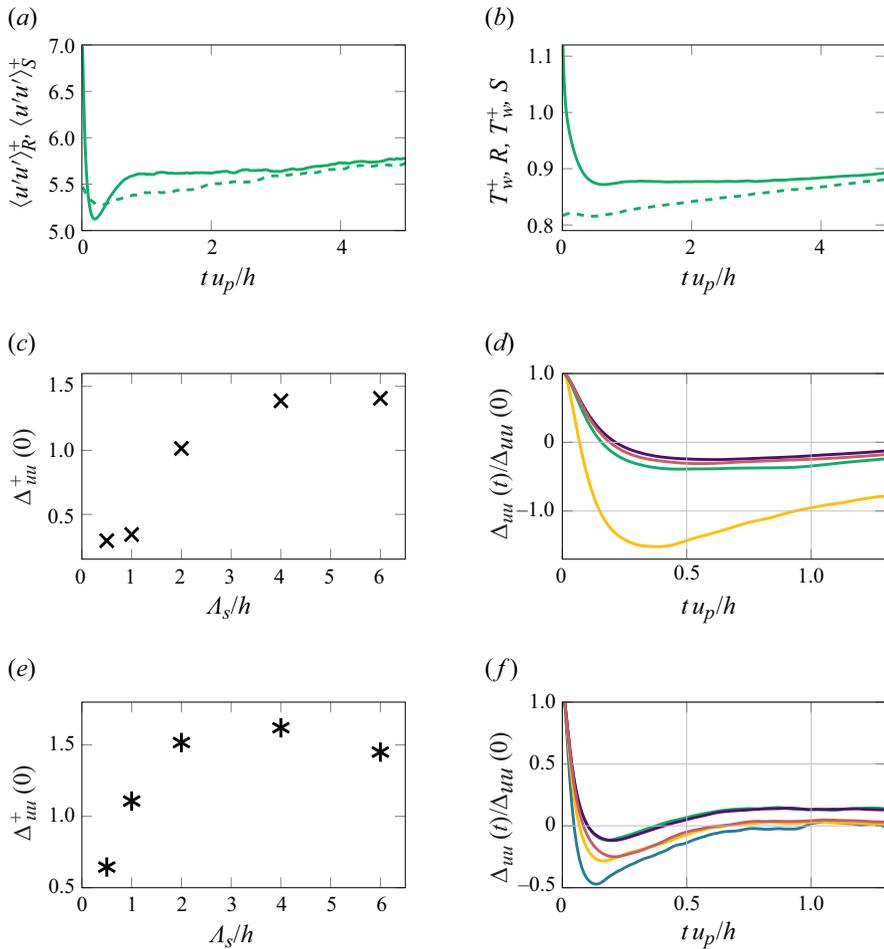
Figure 14. (*a*) Time evolution of $\langle u'u' \rangle_R^+$ (solid) and $\langle u'u' \rangle_S$ (dashed); $Re_\tau = 500$, $\Lambda_s/h = 2$. (*b*) Time evolution of $\tau_{w,R}$ (solid) and $\tau_{w,S}$ (dashed) for the same flow case as panel (*a*). (*c*) Initial values of Δ_{uu}^+ as a function of Λ_s at $Re_\tau = 180$. (*d*) Time evolution of Δ_{uu} at $Re_\tau = 180$. (*e,f*) Same as panels (*c,d*), but at $Re_\tau = 500$. Colour legend as in table 1: ■ $\Lambda_s/h = 0.5$; ■ $\Lambda_s/h = 1$; ■ $\Lambda_s/h = 2$; ■ $\Lambda_s/h = 4$; ■ $\Lambda_s/h = 6$.

ensemble-averaging multiple realisations (simulations) of each considered flow case. To our best knowledge, it is the first time that time-evolving ensemble averages of secondary flows are produced from direct numerical simulation (DNS).

Steady-state data over strip-type roughness are used to highlight the features of the secondary motions, which we investigate both in physical and Fourier space. By comparing the spectra of smooth-wall simulations with those observed over strip-type roughness, we find that a dispersive average correctly isolates the main differences between the two set-ups. The dispersive velocity field captures both the cross-sectional circulatory motions typically associated with secondary motions and the streamwise-momentum pathways observed, for instance, by Barros & Christensen (2014) and Womack *et al.* (2022). We divide the dispersive velocity field into three different regions: a near-wall velocity pattern (closely linked to the wall shear stress), an anti-correlation region and an equilibrium one. The anti-correlation region is the one where the streamwise and wall-normal components of the dispersive velocity ($\tilde{u}$ and $\tilde{v}$, respectively) are indeed anti-correlated; this is also where strong cross-sectional circulatory motions are observed.

In the equilibrium region, instead, the wall-normal profile of the streamwise velocity $U + \tilde{u}$ scaled in local viscous units roughly collapses on the profile observed in spanwise-homogeneous conditions (either over a smooth or a rough wall). The three regions are only clearly distinguishable for large values of Λ_s. Indeed, the secondary motions grow taller in the wall-normal direction for increasing value of Λ_s, so that the anti-correlation region and the near-wall pattern become separated in the wall-normal direction. Moreover, while the anti-correlation region is dominant for small values of Λ_s, it remains confined at roughness transitions (regions of large spanwise gradient of roughness properties) for large values of Λ_s, so that an equilibrium region arises in the middle of each strip. By analysing the budget equation for $\tilde{u}$, we speculate that the $\langle u'v' \rangle$ Reynolds stress is mainly responsible for the formation of the equilibrium region and of the wall shear stress pattern. The formation of the anti-correlation region, instead, appears to be driven by $\tilde{v}$-transport of the mean field U.

We then investigate the time-coherence of the dispersive field once the strip-type roughness is suddenly replaced by smooth walls. A previous study (Kaminaris *et al.* 2023) had indeed highlighted that momentum pathways (here captured by $\tilde{u}$) can sustain for a long streamwise distance in the wake of the rough patch that triggers them. We observe that the time scale T_u describing the decay of the volume-averaged $\tilde{u}$-energy (that is, the overall energy held by the momentum pathways) generally increases with Λ_s. The present data indicate however that the value of T_u might saturate for large Λ_s at the higher tested Reynolds number ($Re_\tau = 500$); further investigation is needed. By converting our temporal information to a spatial one, we provide crude estimates of the streamwise coherence of the momentum pathways ($\Delta x_d \approx 15{-}20\,h$ for $\Lambda_s = 1$, in good agreement with the results of Womack *et al.* 2022). The time scale T_{vw} associated with the circulatory motions also generally increases for increasing Λ_s. Saturation is however observed for $\Lambda_s \geqslant 2$, so that the values of T_{vw} have an upper bound of roughly $2\,h/u_p$; this might be linked to the observed spatial confinement of the circulatory motions (meaning that circulatory motions remain confined to a roughly $2h$-wide region around roughness transitions as Λ_s becomes large). We argue the circulatory motions to be wall-attached; by estimating their half-height, we compare our results with those of Lozano-Durán & Jiménez (2014), who found the lifetime of attached eddies to be proportional to their wall-normal extent. In most considered cases, the momentum pathways take a significantly longer time to decay than the cross-sectional circulatory motions; similarly to the findings of Del Álamo & Jiménez (2006), this suggests that the momentum pathways are mainly, but not exclusively, produced by $\tilde{v}$-transport of U.

The time-coherence of the spanwise wall shear stress pattern is not well captured by the time scale defined with the volume-averaged energy. Such a pattern can be decomposed into the sum of many Fourier modes of spanwise period λ_z. The time to decay of each Fourier mode appears to strongly depend on the wavelength λ_z of the Fourier mode itself and on the Reynolds number, but not much on the global geometry of the flow as captured by the spanwise period Λ_s. Finally, we show that the energy of the fluctuation field found over strip-type roughness is spanwise-heterogeneous; though the fluctuations are random and deprived of any coherent information by definition, their amplitude is coherent with the roughness pattern at the wall. We track these heterogeneities in time.

The aim of this study is to verify the plausibility of the estimates put forward by Townsend (1976) to explain the recurrence of h-scaled flow features in turbulent flows, where h is some outer-layer length scale (here, the channel half-height). Townsend predicted that wall shear stress patterns of a specific characteristic spanwise wavelength ($\lambda_z \approx h$, $\lambda_z \leqslant 4h$) would be able to self-sustain through some induced secondary motion and hence dominate other flow features. We would then expect secondary motions of

A. Andreolli, N. Hutchins, B. Frohnapfel and D. Gatti

a matching period to take the longest time to decay; alternatively, the time to decay could increase as Λ_s grows larger until a threshold value of Λ_s in the range proposed by Townsend is reached. For larger values of Λ_s, the time scale would saturate.

The evidence we gather in reviewing Townsend's estimates is summarised in the following. The analysis of volume-averaged quantities reveals that the time to decay of the cross-sectional circulatory motions saturates for $\Lambda_s / h > 2$, which might be evidence in favour of a weak interpretation of Townsend's hypothesis. The temporal coherence (measured by T_u) of the streamwise-momentum pathways generally increases for increasing Λ_s; however, the present data indicate that saturation might be observed also for the trend of T_u at high Reynolds number. Owing to a relatively high statistical uncertainty, further investigation is needed in this case. Interestingly, the volume-averaged energy I_u of the momentum pathways undergoes a transient growth with respect to its initial value for values of Λ_s in the range $2 \leqslant \Lambda_s / h \leqslant 4$. This transient growth might be evidence that motions of this specific size can self-sustain as proposed by Townsend. An analogy with linear transient growth theory suggests that the growth might be driven by $\tilde{v}$-transport of U; this does not appear to be the case in the present context, though. We are not able to link the time evolution of the circulatory motions (which account for $\tilde{v}$) to the occurence of transient growth. Other mechanisms are likely at play.

Although the gathered evidence is inconclusive, we maintain that Townsend's speculations are plausible. Indeed, the present study considers the temporal decay of fully developed secondary motions which, for large values of Λ_s, become spatially confined to a $2h$-wide region. In these cases, then, we do not effectively study the evolution of a Λ_s-sized structure as intended, but rather of a $2h$-sized one regardless of the value of Λ_s. The confinement itself is evidence in favour of Townsend's idea: the Λ_s-sized perturbation provided by the roughness pattern fails to leverage a secondary motion of comparable size. Instead, some $2h$-sized motions become dominant. The topic could be further investigated, for instance, by studying the evolution of artificial perturbations whose size can be exactly controlled. The perturbations could be then tracked using the methodology proposed in the present paper. If a constant perturbation is applied to different snapshots of the same steady-state flow between smooth walls and the snapshots are allowed to evolve independently, an ensemble average should be able to isolate the evolution of the coherent perturbation. We recommend using a near-wall periodic perturbation applied to the spanwise velocity component: linear analysis suggests that wall-bounded flows are particularly sensitive to such a disturbance (Jovanović & Bamieh 2005). Spanwise positions at which this disturbance is maximum would be equivalent to roughness transitions. Such a set-up could shed light on the mechanisms driving the formation of secondary motions; moreover, it could help to explain why they remain confined at roughness transitions for large values of Λ_s.

Appendix A. Confidence on the occurrence of transient growth

In § 5.1, it was shown that the volume-averaged energy I_u of the streamwise momentum pathways undergoes a temporary increase (transient growth) before decaying to zero as the strip-type roughness is removed from the walls of the channel. The estimates of such volume-averaged energy I_u are affected by statistical uncertainty; the aim of this section is to assess whether the observed transient growth is significant given the statistical uncertainty.

As previously mentioned, the values of I_u reported in this article are estimates of the exact (true) expected value of the volume-averaged streamwise energy; in the following, the value of such a true expected value at a generic point in time t_k will be indicated as $\mathcal{I}_k$. Notice that $\mathcal{I}_k$ is not a random valuable and yet it is not known exactly; the chances of it falling around the value of the estimate $I_u(t_k)$ is described by a probability density function p_k. In light of section § 3.5, p_k is assumed to be a normal distribution with mean $m_k = I_u(t_k)$ and standard deviation $\sigma_k = \mathcal{E}\{I_u\}/2$:

$$p_k(\mathcal{I}_k) = \frac{1}{\sqrt{2\pi\sigma_k^2}} \exp\left(-\frac{(\mathcal{I}_k - m_k)^2}{2\sigma_k^2}\right). \tag{A1}$$

Let now $t_1 = 0$ indicate the initial instant of time at which the flow is at a steady state over strip-type roughness. For $t > t_1$, the strip-type roughness is removed from the walls and the transient growth is observed; let t_2 indicate the instant of time at which I_u has its maximum value, so that $I_u(t_2) > I_u(t_1)$. The statistical significance of the observed transient growth is estimated by calculating the probabilty $P(\mathcal{I}_2 > \mathcal{I}_1)$ that the true value $\mathcal{I}_2$ exceeds the true intial value $\mathcal{I}_1$. The errors on $\mathcal{I}_1$ and $\mathcal{I}_2$ are assumed to be statistically independent, so that the joint probabilty distribution function of $\mathcal{I}_1$ and $\mathcal{I}_2$ is $p_1 p_2$. As an example, the two probability distributions $p_1(\mathcal{I}_1)$ and $p_2(\mathcal{I}_2)$ are reported in figure 15(*a*) for the simulation at $Re_\tau = 500$, $\Lambda_s/h = 4$; the corresponding joint probability density function is shown in panel (*b*). Bear in mind (see the above definition of p_k) that the normal distributions p_1 and p_2 are defined using the estimated value of I_u and its uncertainty (quantified as per § 3.5) at specific instants of time. The probability $P(\mathcal{I}_2 > \mathcal{I}_1)$ can be calculated by integrating the probability density $p_1 p_2$ on the domain highlighted in figure 15(*b*):

$$P(\mathcal{I}_2 > \mathcal{I}_1) = \int_{\mathcal{I}_1 = -\infty}^{+\infty} \int_{\mathcal{I}_2 = \mathcal{I}_1}^{+\infty} p_1(\mathcal{I}_1)\, p_2(\mathcal{I}_2)\, \mathrm{d}\mathcal{I}_2\, \mathrm{d}\mathcal{I}_1 \tag{A2}$$

$$= \int_{-\infty}^{+\infty} p_1(\mathcal{I}_1)\, \frac{1}{2}\, \mathrm{erfc}\left(\frac{\mathcal{I}_1 - m_2}{\sqrt{2}\,\sigma_2}\right) \mathrm{d}\mathcal{I}_1, \tag{A3}$$

where $\mathrm{erfc}(\cdot)$ indicates the complementary error function,

$$\mathrm{erfc}(x) = 1 - \mathrm{erf}(x) = \frac{2}{\sqrt{\pi}} \int_x^{+\infty} \exp\left(-t^2\right)\, \mathrm{d}t. \tag{A4}$$

(*a*)   (*b*)
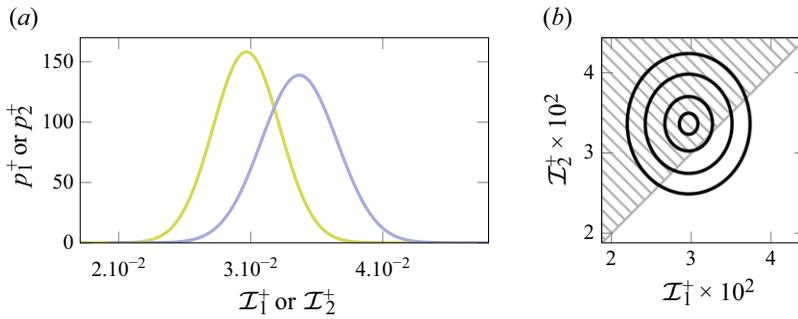
Figure 15. (*a*) Probability density functions $p_1(\mathcal{I}_1)$ (green) and $p_2(\mathcal{I}_2)$ (blue) for the simulation at $Re_\tau = 500$, $\Lambda_s/h = 4$. (*b*) Contours (1 %, 10 %, 50 % and 90 % of the maximum value) of the joint probability density function $p_1 p_2$; the hatched area indicates the integration domain $\mathcal{I}_2 > \mathcal{I}_1$ used in (A2) to calculate $P(\mathcal{I}_2 > \mathcal{I}_1)$.

The above procedure is used to estimate the confidence on the occurrence of transient growth for the two high-Re simulations ($Re_\tau = 500$) with $\Lambda_s/h = 2$ and $\Lambda_s/h = 4$. The confidence reads 78.9 % and 85.2 %, respectively.

Appendix B. Localising excess energy in space

The analysis of § 5.1, which is based on volume-averaged quantities, indicates that a net increase of the overall (volume-averaged) kinetic energy associated with the momentum pathways is observed under given circumstances. In this section, an attempt to better localise this excess energy will be done. This is done by scrutinising the change $\Delta \tilde{u}^2/2$ in the dispersive streamwise kinetic energy $\tilde{u}^2/2$ at a given time t with respect to its initial steady-state value ($t = 0$):

$$\Delta \frac{\tilde{u}^2}{2}(t, y, \zeta) = \frac{\tilde{u}^2}{2}(t, y, \zeta) - \frac{\tilde{u}^2}{2}(0, y, \zeta). \tag{B1}$$

Positive values of $\Delta \tilde{u}^2/2$ at a given (y, ζ)-position indicate that an excess of energy is seen there with respect to the initital conditions. Notice that localised regions of excess energy can simply ensue as a result of transport processes (e.g. energy is transported from a region to another, so that the former is depleted of its energy, whereas the energy of the latter grows). Transport processes cannot yield a net energy increase, i.e. an increase of the volume-averaged energy.

Figure 16 shows the (y, ζ)-distribution of $\Delta \tilde{u}^2/2$ at some selected instants of time for selected values of Λ_s and $Re_\tau = 500$. For $\Lambda_s/h = 0.5$, no global energy transient growth was observed in § 5.1; however, some localised excess energy is seen right above $y^+ \approx 10$ (panels *a, b*) during the decay of the secondary motions, whereas the region below $y^+ \approx 10$ shows an energy deficit. Two explanations are possible. Perhaps, some transport process (e.g. viscous diffusion, see § 5.2) transports energy upwards from the near-wall region; alternatively, separate processess might be providing energy to the region above $y^+ \approx 10$ and extracting a larger amount of energy from the $y^+ < 10$ region. Overall, the net effect is a decrease of the global $\tilde{u}^2/2$ energy, coherently with the volume-averaged energy trends of figure 8(*g*).

Data for $\Lambda_s/h = 2$ are shown in figure 16(*d–f*). Notice that a transient growth of the volume-averaged energy I_u is seen for this case (see § 5.1). At the beginning of the decay, some excess energy is seen right above $y^+ = 10$ similarly to panels (*a,b*); at the time of the maximum transient growth of I_u (panel *e*), much more excess energy is found around
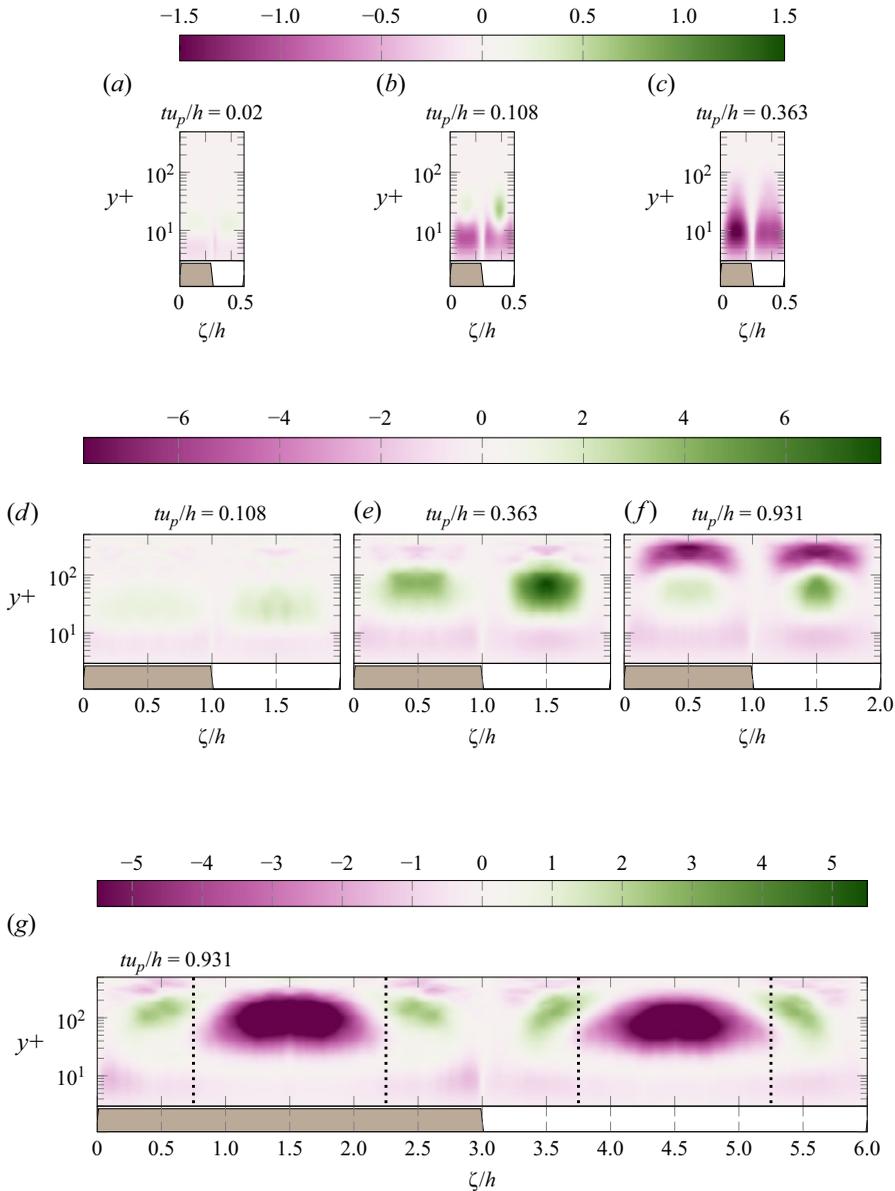
Figure 16. Premultiplied energy difference $y^+(\Delta \tilde{u}^2/2)^+$ at a given instant of time t (reported above each panel); data at $Re_\tau = 500$. (a–c) $\Lambda_s/h = 0.5$. (d–f) $\Lambda_s/h = 2$; Panel (e) shows data at the instant of time for which maximum transient growth is observed for this value of Λ_s. (g) $\Lambda_s/h = 6$. Below each panel, a grey fill indicates portions of the wall that were rough at the initial condition; the vertical dotted lines mark the boundaries of the anti-correlation and equilibrium regions.

$40 < y^+ < 100$. As time progresses, the excess energy is still seen in that region; however, a significant amount of energy is lost further away from the wall.

Interestingly, an excess of energy around $y^+ \approx 100 - 200$ is also seen for $\Lambda_s/h = 6$ (figure 16g), although it is localised to the anti-correlation region (that is, around roughness transitions; see § 3.3). By contrast, the remaining part of the channel (that is, the equilibrium region) quickly loses its energy. As a rough approximation, for the
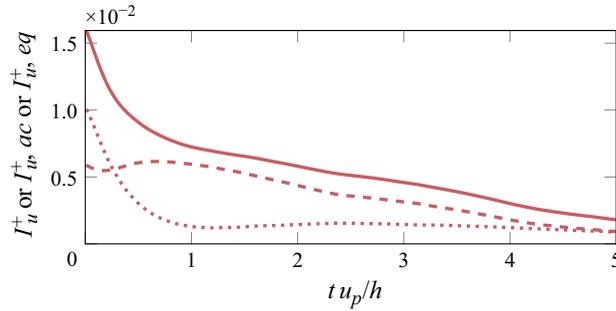
Figure 17. $Re_\tau = 500$, $\Lambda_s/h = 6$. Time-evolution of the volume-averaged energy of the momentum pathways: overall (I_u, solid), conditionally averaged in the anti-correlation region ($I_{u,ac}$, dashed) and in the equilibrium region ($I_{u,eq}$, dotted).

present context, we consider the anti-correlation region to be found in a $1.5h$-wide region around roughness transitions (notice that we used a slightly different definition in § 4); two vertical lines in panel (*g*) mark such an approximated border. In an attempt to shed light on whether the excess energy seen in the anti-correlation region might be linked to a net energy increase in the same region, we define the volume-averaged energy $I_{u,ac}$ of the anticorrelation region and that $I_{u,eq}$ of the equilibrium region. The two are defined so that $I_{u,ac} + I_{u,eq} = I_u$; all of these three time signals are reported in figure 17. The energy $I_{u,eq}$ of the equilibrium region quickly decays, so that for $t\,u_p/h \geqslant 1$, the overall volume-averaged energy is dominated by the energy $I_{u,ac}$ of the anti-correlation region. Interestingly, $I_{u,ac}$ appears to undergo a mild transient growth; surely, it mantains a roughly constant energy level for $t\,u_p/h \leqslant 1$.

In a sense, then, we observe transient growth of the (conditionally averaged) energy of the momentum pathways for the large strip width $\Lambda_s/h = 6$. This might appear to be evidence against Townsend's hypothesis, as self-sustainment of the secondary motions would be expected for narrower strip widths (e.g. $2 \leqslant \Lambda_s/h \leqslant 4$). In fact, it is not. The circulatory motions that ensue for $\Lambda_s/h = 6$ are spatially confined (see § 4); their size (twice the width of a confined circulatory motion, for consistency) is smaller than the period $\Lambda_s/h = 6$ of the roughness pattern, and falls in the range proposed by Townsend.

REFERENCES

ALIZARD, F., PIROZZOLI, S., BERNARDINI, M. & GRASSO, F. 2015 Optimal transient growth in compressible turbulent boundary layers. *J. Fluid Mech.* **770**, 124–155.
ANDERSON, W., BARROS, J.M., CHRISTENSEN, K.T. & AWASTHI, A. 2015 Numerical and experimental study of mechanisms responsible for turbulent secondary flows in boundary layer flows over spanwise heterogeneous roughness. *J. Fluid Mech.* **768**, 316–347.
ANDREOLLI, A., GATTI, D., VINUESA, R., ÖRLÜ, R. & SCHLATTER, P. 2023 Separating large-scale superposition and modulation in turbulent channels. *J. Fluid Mech.* **958**, A37.
BAARS, W.J., HUTCHINS, N. & MARUSIC, I. 2017 Self-similarity of wall-attached turbulence in boundary layers. *J. Fluid Mech.* **823**, R2.
BARROS, J.M. & CHRISTENSEN, K.T. 2014 Observations of turbulent secondary flows in a rough-wall boundary layer. *J. Fluid Mech.* **748**, R1.
BARROS, J.M. & CHRISTENSEN, K.T. 2019 Characteristics of large-scale and superstructure motions in a turbulent boundary layer overlying complex roughness. *J. Turbul.* **20** (2), 147–173.
BARTHOLOMEW, P., DESKOS, G., FRANTZ, R.A., SCHUCH, F.N., LAMBALLAIS, E. & LAIZET, S. 2020 Xcompact3D: an open-source framework for solving turbulence problems on a Cartesian mesh. *SoftwareX* **12**, 100550.
BILLINGSLEY, P. 1995 Probability and measure. In *Wiley Series in Probability and Mathematical Statistics*. 3rd edn. Wiley.

CHUNG, D., HUTCHINS, N., SCHULTZ, M.P. & FLACK, K.A. 2021 Predicting the drag of rough surfaces. *Annu. Rev. Fluid Mech.* **53** (1), 439–471.

CHUNG, D., MONTY, J.P. & HUTCHINS, N. 2018 Similarity and structure of wall turbulence with lateral wall shear stress variations. *J. Fluid Mech.* **847**, 591–613.

COSSU, C., PUJALS, G. & DEPARDON, S. 2009 Optimal transient growth and very large–scale structures in turbulent boundary layers. *J. Fluid Mech.* **619**, 79–94.

CRAMERI, F. 2023 *Scientific Colour Maps*. Zenodo.

CRAMERI, F., SHEPHARD, G.E. & HERON, P.J. 2020 The misuse of colour in science communication. *Nat. Commun.* **11** (1), 5444.

DAVIDSON, P. 2015 *Turbulence: An Introduction for Scientists and Engineers*. 2nd edn. Oxford University Press.

DEL ÁLAMO, J.C. & JIMÉNEZ, J. 2006 Linear energy amplification in turbulent channels. *J. Fluid Mech.* **559**, 205.

FLACK, K.A. & SCHULTZ, M.P. 2010 Review of hydraulic roughness scales in the fully rough regime. *J. Fluids Engng* **132** (4), 041203.

FLORES, O. & JIMÉNEZ, J. 2010 Hierarchy of minimal flow units in the logarithmic layer. *Phys. Fluids* **22** (7), 071704.

FROHNAPFEL, B., VON DEYN, L., YANG, J., NEUHAUSER, J., STROH, A., ÖRLÜ, R. & GATTI, D. 2024 Flow resistance over heterogeneous roughness made of spanwise-alternating sandpaper strips. *J. Fluid Mech.* **980**, A31.

GATTI, D., STROH, A., FROHNAPFEL, B. & HASEGAWA, Y. 2018 Predicting turbulent spectra in drag-reduced flows. *Flow Turbul. Combust.* **100** (4), 1081–1099.

HINZE, J.O. 1967 Secondary currents in wall turbulence. *Phys. Fluids* **10** (9), S122–S125.

HUTCHINS, N. & MARUSIC, I. 2007a Evidence of very long meandering features in the logarithmic region of turbulent boundary layers. *J. Fluid Mech.* **579**, 1–28.

HUTCHINS, N. & MARUSIC, I. 2007b Large-scale influences in near-wall turbulence. *Phil. Trans. R. Soc. Lond. A: Math. Phys. Engng Sci.* **365** (1852), 647–664.

HWANG, H.G. & LEE, J.H. 2018 Secondary flows in turbulent boundary layers over longitudinal surface roughness. *Phys. Rev. Fluids* **3** (1), 014608.

HWANG, J., LEE, J., SUNG, H.J. & ZAKI, T.A. 2016 Inner–outer interactions of large-scale structures in turbulent channel flow. *J. Fluid Mech.* **790**, 128–157.

HWANG, Y. & COSSU, C. 2010 Linear non-normal energy amplification of harmonic and stochastic forcing in the turbulent channel flow. *J. Fluid Mech.* **664**, 51–73.

ILLINGWORTH, S.J. 2020 Streamwise-constant large-scale structures in Couette and Poiseuille flows. *J. Fluid Mech.* **889**, A13.

JOVANOVIĆ, M.R. & BAMIEH, B. 2005 Componentwise energy amplification in channel flows. *J. Fluid Mech.* **534**, 145–183.

KAMINARIS, I.K., BALARAS, E., SCHULTZ, M.P. & VOLINO, R.J. 2023 Secondary flows in turbulent boundary layers developing over truncated cone surfaces. *J. Fluid Mech.* **961**, A23.

KEVIN, K., MONTY, J. & HUTCHINS, N. 2019 The meandering behaviour of large-scale structures in turbulent boundary layers. *J. Fluid Mech.* **865**, R1.

KEVIN, K., MONTY, J.P., BAI, H.L., PATHIKONDA, G., NUGROHO, B., BARROS, J.M., CHRISTENSEN, K.T. & HUTCHINS, N. 2017 Cross-stream stereoscopic particle image velocimetry of a modified turbulent boundary layer over directional surface pattern. *J. Fluid Mech.* **813**, 412–435.

KIM, K.C. & ADRIAN, R.J. 1999 Very large-scale motion in the outer layer. *Phys. Fluids* **11** (2), 417–422.

KLINE, S.J., REYNOLDS, W.C., SCHRAUB, F.A. & RUNSTADLER, P.W. 1967 The structure of turbulent boundary layers. *J. Fluid Mech.* **30** (4), 741–773.

LAIZET, S. & LAMBALLAIS, E. 2009 High-order compact schemes for incompressible flows: a simple and efficient method with quasi-spectral accuracy. *J. Comput. Phys.* **228** (16), 5989–6015.

LAIZET, S. & LI, N. 2011 Incompact3d: a powerful tool to tackle turbulence problems with up to O (10^5) computational cores. *Intl J. Numer. Meth. Flow* **67** (11), 1735–1757.

LEE, M. & MOSER, R.D. 2015 Direct numerical simulation of turbulent channel flow up to. *J. Fluid Mech.* **774**, 395–415.

LEE, M. & MOSER, R.D. 2018 Extreme-scale motions in turbulent plane Couette flows. *J. Fluid Mech.* **842**, 128–145.

LEHEW, J.A., GUALA, M. & MCKEON, B.J. 2013 Time-resolved measurements of coherent structures in the turbulent boundary layer. *Exp. Fluids* **54** (4), 1508.

LOZANO-DURÁN, A. & JIMÉNEZ, J. 2014 Time-resolved evolution of coherent structures in turbulent channels: characterization of eddies and cascades. *J. Fluid Mech.* **759**, 432–471.

LUCHINI, P., MANZO, F. & POZZI, A. 1991 Resistance of a grooved surface to parallel flow and cross-flow. *J. Fluid Mech. Digital Arch.* **228**, 87.

MARUSIC, I. & MONTY, J.P. 2019 Attached Eddy model of wall turbulence. *Annu. Rev. Fluid Mech.* **51** (1), 49–74.

MATHIS, R., HUTCHINS, N. & MARUSIC, I. 2009 Large-scale amplitude modulation of the small-scale structures in turbulent boundary layers. *J. Fluid Mech.* **628**, 311–337.

MEDJNOUN, T., VANDERWEL, C. & GANAPATHISUBRAMANI, B. 2018 Characteristics of turbulent boundary layers over smooth surfaces with spanwise heterogeneities. *J. Fluid Mech.* **838**, 516–543.

MEDJNOUN, T., VANDERWEL, C. & GANAPATHISUBRAMANI, B. 2020 Effects of heterogeneous surface geometry on secondary flows in turbulent boundary layers. *J. Fluid Mech.* **886**, A31.

MEJIA-ALVAREZ, R., BARROS, J.M. & CHRISTENSEN, K.T. 2013 Structural attributes of turbulent flow over a complex topography. In *Coherent Flow Structures at Earth's Surface*. 1st edn (ed. J.G., VENDETTI, J.L., BEST, CHURCH, M. & HARDY, R.J.), pp. 25–41. Wiley.

MEJIA-ALVAREZ, R. & CHRISTENSEN, K.T. 2013 Wall-parallel stereo particle-image velocimetry measurements in the roughness sublayer of turbulent flow overlying highly irregular roughness. *Phys. Fluids* **25** (11), 115109.

NEUHAUSER, J., SCHÄFER, K., GATTI, D. & FROHNAPFEL, B. 2022 Simulation of turbulent flow over roughness strips. *J. Fluid Mech.* **945**, A14.

NIKORA, V.I., STOESSER, T., CAMERON, S.M., STEWART, M., PAPADOPOULOS, K., OURO, P., MCSHERRY, R., ZAMPIRON, A., MARUSIC, I. & FALCONER, R.A. 2019 Friction factor decomposition for rough-wall flows: theoretical background and application to open-channel flows. *J. Fluid Mech.* **872**, 626–664.

NIKURADSE, J. 1931 Strömungswiderstand in rauhen Rohren. *Z. Angew. Math. Mech.* **11** (6), 409–411.

NUGROHO, B., HUTCHINS, N. & MONTY, J. 2013 Large-scale spanwise periodicity in a turbulent boundary layer induced by highly ordered and directional surface roughness. *Intl J. Heat Fluid Flow* **41**, 90–102.

REYNOLDS, R.T., HAYDEN, P., CASTRO, I.P. & ROBINS, A.G. 2007 Spanwise variations in nominally two-dimensional rough-wall boundary layers. *Exp. Fluids* **42** (2), 311–320.

REYNOLDS, W.C. & HUSSAIN, A.K.M.F. 1972 The mechanics of an organized wave in turbulent shear flow. Part 3. Theoretical models and comparisons with experiments. *J. Fluid Mech.* **54** (2), 263–288.

SCHÄFER, K. 2023 Turbulent large-scale structures over heterogeneous surfaces. PhD thesis, Karlsruhe Institute for Technology (KIT), Kalsruhe, Germany.

STROH, A., HASEGAWA, Y., KRIEGSEIS, J. & FROHNAPFEL, B. 2016 Secondary vortices over surfaces with spanwise varying drag. *J. Turbul.* **17** (12), 1142–1158.

STROH, A., SCHÄFER, K., FROHNAPFEL, B. & FOROOGHI, P. 2020 Rearrangement of secondary flow over spanwise heterogeneous roughness. *J. Fluid Mech.* **885**, R5.

TOH, S. & ITANO, T. 2005 Interaction between a large-scale structure and near-wall structures in channel flow. *J. Fluid Mech.* **524**, 249–262.

TOWNSEND, A.A. 1976 The structure of turbulent shear flow, 2nd edn.

TÜRK, S., DASCHIEL, G., STROH, A., HASEGAWA, Y. & FROHNAPFEL, B. 2014 Turbulent flow over superhydrophobic surfaces with streamwise grooves. *J. Fluid Mech.* **747**, 186–217.

VANDERWEL, C. & GANAPATHISUBRAMANI, B. 2015 Effects of spanwise spacing on large-scale secondary flows in rough-wall turbulent boundary layers. *J. Fluid Mech.* **774**, R2.

VANDERWEL, C., STROH, A., KRIEGSEIS, J., FROHNAPFEL, B. & GANAPATHISUBRAMANI, B. 2019 The instantaneous structure of secondary flows in turbulent boundary layers. *J. Fluid Mech.* **862**, 845–870.

WANG, Z.-Q. & CHENG, N.-S. 2006 Time-mean structure of secondary flows in open channel with longitudinal bedforms. *Adv. Water Resour.* **29** (11), 1634–1649.

WANGSAWIJAYA, D. & HUTCHINS, N. 2022 Investigation of unsteady secondary flows and large-scale turbulence in heterogeneous turbulent boundary layers. *J. Fluid Mech.* **934**, A40.

WANGSAWIJAYA, D.D., BAIDYA, R., CHUNG, D., MARUSIC, I. & HUTCHINS, N. 2020 The effect of spanwise wavelength of surface heterogeneity on turbulent secondary flows. *J. Fluid Mech.* **894**, A7.

WILLINGHAM, D., ANDERSON, W., CHRISTENSEN, K.T. & BARROS, J.M. 2014 Turbulent boundary layer flow over transverse aerodynamic roughness transitions: induced mixing and flow characterization. *Phys. Fluids* **26** (2), 025111.

WOMACK, K.M., VOLINO, R.J., MENEVEAU, C. & SCHULTZ, M.P. 2022 Turbulent boundary layer flow over regularly and irregularly arranged truncated cone surfaces. *J. Fluid Mech.* **933**, A38.

YANG, J., STROH, A., LEE, S., BAGHERI, S., FROHNAPFEL, B. & FOROOGHI, P. 2023 Prediction of equivalent sand-grain size and identification of drag-relevant scales of roughness – a data-driven approach. *J. Fluid Mech.* **975**, A34.

ZAMPIRON, A., CAMERON, S. & NIKORA, V. 2020 Secondary currents and very-large-scale motions in open-channel flow over streamwise ridges. *J. Fluid Mech.* **887**, A17.